Check for
updates

On-Chip Electrical Monitoring of Real-Time "Soft" and "Hard" Protein Corona Formation on Carbon Nanoparticles

Indrajit Srivastava, Muhammad S. Khan, Ketan Dighe, Maha Alafeef, Zhen Wang, Tuseeta Banerjee, Tanmay Ghonge, Lauren M. Grove, Rashid Bashir, and Dipanjan Pan*

When nanoparticles encounter a biological fluid, proteins, lipids, and other biomolecules adsorb on the nanoscale surface consequently leading to the evolution of a protein shell or "corona." The corona formed is dynamic in nature and depends on the "synthetic identity" of the NPs, ultimately affecting their biological response. In this paper, an integrated microfluidic platform coupled with an electrical resistance measurement setup is developed to monitor and investigate the real-time formation of a biomolecular corona of carbon nanoparticles. "Soft" and "hard" corona formation stages are effectively discriminated based on their nanoscale surface chemistries when combined with a time-frequency tool known as wavelet transform and machine-learning techniques. Additionally, the corona and its composition are studied using different techniques such as dynamic light scattering, nanoparticle tracking analysis, zeta potential, excitation–emission profiles, 1D sodium dodecyl polyacrylamide gel electrophoresis and subsequently, liquid chromatography-mass spectrometry analysis. The dynamic setup can eventually be used as a valuable tool for screening of any nanoparticles formulations with distinct surface chemistries for the purpose of reduced protein adsorption/weaker protein corona formation and consequently enhance the success of targeted drug delivery.

1. Introduction

Upon incubation of nanoparticles (NPs) in biological fluids, proteins, lipids, and other biomolecules rapidly compete for binding at the nanoscale surface, leading to the formation of a dynamic protein "corona."[1–3] This corona is generally described as a two-component system consisting of a tightly bound inner layer, called as "hard" corona, whereas an outer layer of loosely associated proteins is called as "soft" corona. Furthermore, in the "hard" protein corona, proteins interact directly with the NP surface via long-range, strong protein–surface interactions, unlike in the case of "soft" corona where proteins interact with other proteins using shot-range, protein–protein interactions.[4,5] It has been found that the earlier step is often followed by secondary step that leads to a protein mediated NPs agglomeration/aggregation, which have been found to affect several in vitro and in vivo experiments.[6–9] The protein binding

I. Srivastava, Dr. M. S. Khan, K. Dighe, M. Alafeef, Z. Wang,
Dr. T. Ghonge, L. M. Grove, Prof. R. Bashir, Prof. D. Pan
Department of Bioengineering
University of Illinois at Urbana-Champaign
Urbana, IL 61801, USA
E-mail: dipanjan@illinois.edu, dipanjan@som.umaryland.edu

I. Srivastava, Dr. M. S. Khan, K. Dighe, M. Alafeef, Z. Wang,
Dr. T. Ghonge, L. M. Grove, Prof. R. Bashir, Prof. D. Pan
Mills Breast Cancer Institute
Carle Foundation Hospital
Urbana, IL 61801, USA

M. Alafeef
Biomedical Engineering Department
Jordan University of Science and Technology
Irbid 21110, Jordan

Dr. T. Banerjee
lfram Research Inc., Champaign
Urbana, IL 61801, USA

Dr. T. Ghonge, Prof. R. Bashir
Micro and Nanotechnology Lab
University of Illinois at Urbana-Champaign
Urbana, IL 61801, USA

Prof. R. Bashir, Prof. D. Pan
Carle Illinois College of Medicine
807 South Wright St., Urbana, IL 61801, USA

Prof. D. Pan
Beckman Institute
University of Illinois at Urbana-Champaign
Urbana, IL 61801, USA

Prof. D. Pan
Department of Materials Science and Engineering
University of Illinois at Urbana-Champaign
Urbana, IL 61801, USA

Prof. D. Pan
Departments of Diagnostic Radiology and Nuclear Medicine
and Pediatrics
University of Maryland Baltimore
Health Sciences Facility III
670 W Baltimore St., Baltimore, MD 21201, USA

Prof. D. Pan
Department of Chemical
Biochemical and Environmental Engineering
University of Maryland Baltimore County
Interdisciplinary Health Sciences Facility
1000 Hilltop Circle Baltimore, Baltimore, MD 21250, USA

ADVANCED
SCIENCE NEWS
www.advancedsciencenews.com

small
methods
www.small-methods.com

is energetically favorable as it reduces the surface energy of the NP, removing the hydration layer surrounding it and increasing its entropy. The protein corona complex so formed defines the biological identity of the particles, consequently affecting its biophysical properties such that they differ widely from the as-synthesized particle. Furthermore, the particle's biodistribution as well biological response could be influenced due to the corona formation sometimes leading to unwanted biological side-effects.[10–13] Owing to the significance of these protein corona complexes, various experimental techniques have been developed and employed to study them over the last decade.[14–19] These consist of both direct methods, which directly analyze the proteins adsorbed onto the NP surface or indirect methods, in which knowledge about the protein corona complex is gained by measuring the changes in properties of the NPs. Direct methods could be used to collect information such as structural identity (via circular dichroism, nuclear magnetic resonance (NMR) spectroscopy, Fourier transform infrared FTIR spectroscopy, etc.) quantification (via transmission electron microscopy (TEM), protein assays, etc.) and identification (via sodium dodecyl polyacrylamide gel electrophoresis (SDS-PAGE) and mass spectroscopy. Indirect methods have been used to gather structural and conformational information via dynamic light scattering (DLS) and fluorescence correlation spectroscopy (FCS). Utilizing the techniques, recent reports have confirmed that physiochemical properties such as size, shape, surface chemistry, particle material, etc. play a crucial role in determining the composition of the corona.[20–28] In addition to NPs properties, the concentration of proteins in biological medium also play a critical role in formation of corona.[29] Out of the above discussed physiochemical properties, "synthetic identity" or surface chemistry of a nanoparticle is regarded as one of the most influencing factors for determining their biological performances which govern the interaction of NPs with biomolecules in the environment. A detailed understanding of the impetus surface functionalization plays on the biological effects of NPs is needed to develop a potential strategy to facilitate efficient engineering of NPs for nanomedicine. Most of the in vitro protein corona studies until now have been limited to static conditions where incubation of NPs in biological fluids such as serum, plasma, etc. in a centrifuge tube for a fixed amount of time followed by studying the composition of the corona using proteomic analysis.[30,31] This, however, is not a real representation of a systemic physiological scenario. A more realistic case would involve the dynamic nature of blood flow and formation of a protein corona developed under a fluidic flow using a microfluidic device analogous to a physiological environment as conducted by some recent studies.[32–35] However, most of these works used the microfluidic device either as a dynamic incubation environment or coupled with analytical techniques. Although a combination of an analytical method and microfluidics provides versatile technique to study protein corona, they are costly, time intensive, and require large stationary-equipment and reagents to perform the said technique. These restrictions become a major hurdle for situations with resource scarcity.

Herein, we have developed an integrated microfluidic platform coupled with an electrical resistance measurement setup to monitor the real-time formation of a biomolecular corona of carbon nanoparticles (CNPs) (**Figure 1**a) having different surface charges (such as anionic, cationic, neutral, and zwitterionic) in a time-resolved manner. By employing ML tools and wavelet transform (WT) techniques, we effectively discriminated against "soft" versus "hard" corona formation based on nanoscale surface chemistries. This could potentially lead to the visualization of the types of corona formation process more rapidly (as fast as ≈1 h) and eventually extended across different nanoparticle platforms. We further attempted to correlate and comment on the fouling behavior, i.e., low-fouling versus high-fouling for different CNPs employed in this work based on their varying surface chemistries (zwitterionic lipid, polyethylene glycol (PEG)ylated, and polyethyleneimine (PEI)). Low-fouling surface molecules are critical in drug delivery purposes owing to their reduced protein adsorption and could be used as passivating agents for nanoparticles. Hence, our platform could eventually be used for rapid screening of potential surface passivating molecules for drug delivery purposes. A distinct advantage of using a microfluidic based approach over conventional in situ measurements is the ability to create a dynamic environment with precise control over fluid flow allowing shear force being imposed on NPs and proteins resulting in their rigorous mixing thereby simulating a realistic biological milieu.[36–38] We hypothesize that plasma proteins are the major contributor of the charge carriers (by releasing their free counterions in the solution) and hence will be the bulk contributor toward the conductivity of the solution flowing through a microfluidic device. Interaction of CNPs with the plasma proteins will lead to absorption of the latter onto the nanoscale surface of CNPs forming a protein corona complex that confines the counterions released due to absorption process and consequently lowers the number of effective charge carriers in the solution. This interaction would result in a decrease in electrical conductivity (σ), which in turn would increase the electrical resistance (R) of the solution flowing through the microfluidic channels and respective sections (Figure 1). Our results show that NPs with cationic head-groups form a thicker hard corona whereas NPs with neutral and zwitterion surface groups formed a weaker hard corona owing to their low fouling properties. In addition to this, we applied a time-frequency tool known as WT on the collected real-time resistance data to gain further insights into the protein adsorption and desorption events occurring on the surface of NPs due to their varied surface chemistry. The fabricated microfluidic device was incubated with Coomassie dye and different regions were visualized using an optical microscope to demonstrate successful fabrication (Figure 1b–d).

Results obtained by utilizing our integrated microfluidic system at different time intervals coupled with ML algorithms and WT were compared with standard current techniques. This allowed us to investigate the outcome of the proposed real-time recording and helped evaluate the variations of protein corona formation procedure within different characterization techniques. We anticipate that controlling the adsorption of proteins on NPs by tailoring the chemical motifs at its surface in a dynamic setup will allow a more precise prediction of the protein corona formation process and would be a valuable tool with promising therapeutic benefits in drug delivery and targeted cancer treatment.
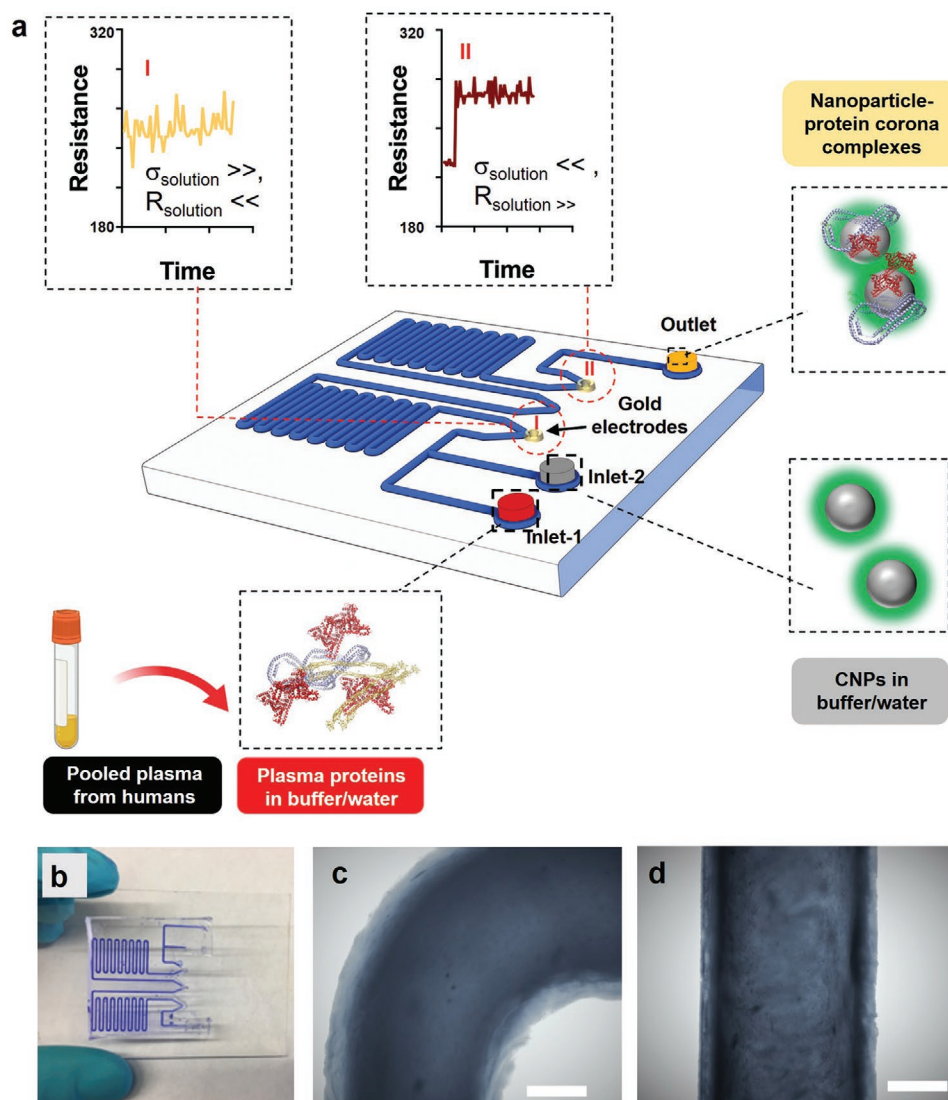
Figure 1. a) Schematic of the microfluidic device used for monitoring the protein corona formation. Using the two inlets, pooled human plasma dispersed in buffer and CNPs were injected and pushed through the device via syringes and allowed to incubate in the serpentine channels for 1 h. The two gold electrodes (highlighted) were employed to record the real-time impedance of the flowing solution before and after an incubation period, following which the nanoparticle–protein complexes were collected from the outlet. b) Fabricated microfluidic device (without Au electrodes) incubated with Coomassie dye to show the microfluidic channels. c,d) Optical micrographs of the different regions of the microfluidic device incubated with Coomassie dye. Each scale bar corresponds to 100 μm.

2. Results and Discussion

2.1. Synthesis of CNPs

CNPs were selected as model NPs due to their relative ease of synthesis along with surface modifications.[39] Pristine/bare CNPs were synthesized from sucrose, a disaccharide composed of two monosaccharides, glucose, and fructose. To investigate the effects of different surface charges and surface chemistry on the protein corona formation, the surface of the carbon core was passivated with either linear or branched organic macromolecules for the synthesis of both pre and postpassivated CNPs. To impart cationic, neutral, and zwitterion functionality, nanoparticle surface was passivated with PEI, PEG,

and lecithin from soy (Zw), respectively. Pristine CNPs, due to presence of carboxylic and hydroxyl groups as observed from X-ray photoelectron spectroscopy (XPS) spectroscopy and FTIR spectroscopy were considered anionic (Figure S8, Supporting Information).[40,41] These were subjected to several preliminary physio-chemical characterization techniques including TEM, UV–vis spectroscopy, X-ray photoelectron spectroscopy and zeta potential measurements (Figures S1–S7 and Table S1, Supporting Information) to confirm their structural integrity. We also demonstrated that as-synthesized CNPs were stable for the duration of the experiments by monitoring their hydrodynamic diameters and zeta potential measurements over a period of 6 days (Figures S9 and S10, Supporting Information).
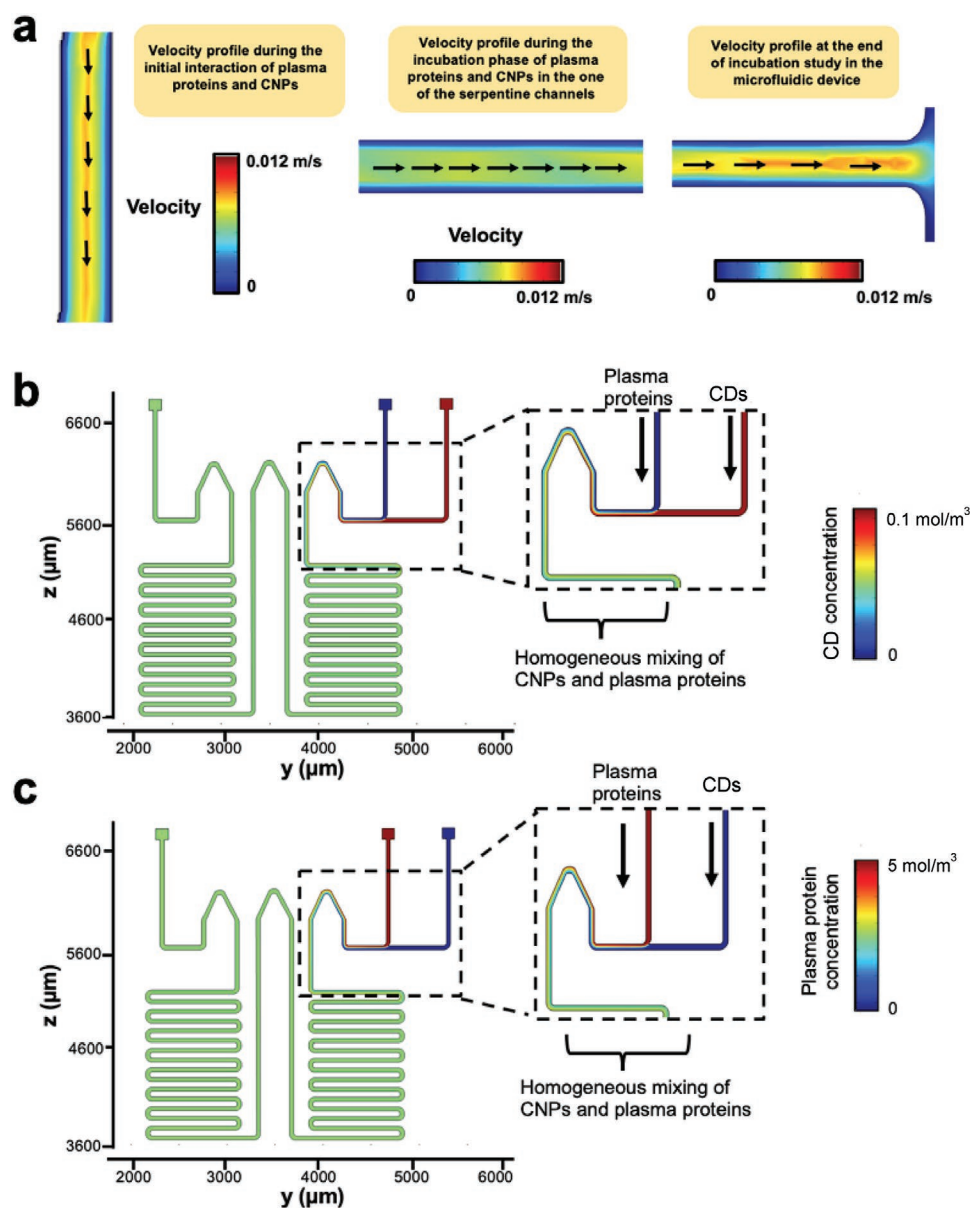
**ADVANCED
SCIENCE NEWS**

www.advancedsciencenews.com

**small
methods**

www.small-methods.com

Figure 2. a) COMSOL generated images for fluid velocity in the microfluidic device at different locations in the microchannel with both plasma proteins and CNPs injected at 1.5 µL min⁻¹. b) COMSOL simulations showing the CNP concentration in the microfluidic channel with the concentration at the inlet (right) is 5 mol m⁻³ (5 × 10⁻³ M). c) COMSOL simulations showing the plasma protein concentration in the microfluidic channel with the concentration at the inlet (left) is 0.1 mol m⁻³ (100 × 10⁻⁶ M). b,c) Plasma proteins and CNPs quickly diffuse and rapidly fill the majority of the microchannel in a homogeneous manner.

2.2. Theoretical Prediction of Velocity and Concentration Profiles in the Microfluidic Channel via COMSOL Simulations

Prior to performing the incubation experiments in the device, to generate their velocity profiles (**Figure 2**a and Figure S11, Supporting Information) within the microfluidic channels as well as concentration profiles for both plasma proteins and CNPs (Figure 2b,c), simulation was performed using COMSOL v5.2 0.[42–44] A multiphysics model was developed using "Laminar Flow" module in COMSOL. The problem being addressed is the result of two physical phenomena taking place

simultaneously. First, the plasma proteins and CNPs solutions flowing in the channel and, secondly, their diffusion across the microfluidic channel. We modeled the flow of plasma and nanoparticle solution as viscous, Newtonian fluid whose behavior is governed by the Navier–Stokes Equation (1)

$$\rho \left(\frac{\partial u}{\partial t} + u \cdot \nabla u \right) = -\nabla p + \nabla^2 u \tag{1}$$

where ρ is density, μ is viscosity, u is velocity vector, and p is pressure.

**ADVANCED
SCIENCE NEWS**

www.advancedsciencenews.com

**small
methods**

www.small-methods.com

Diffusion of different species was modeled by the general convection–diffusion Equation (2), however in case of stationary convection–diffusion equation, the steady state behavior of the convective-diffusive system was employed, meaning $\frac{\partial u}{\partial t} = 0$, so we get Equation (3). Further, since D is a constant, we get Equation (4)

$$\frac{\partial c}{\partial t} = D \nabla c - v \cdot \nabla c \tag{2}$$

$$0 = \nabla \cdot (D \cdot \nabla c) - \nabla (vc) + R \tag{3}$$

$$0 = D \nabla^2 c - \nabla (vc) \tag{4}$$

where D is diffusivity or diffusion coefficient, c is the variable of interest (species concentration for mass transfer), v is the velocity, R is sources of sinks, and taken as 0 for this case.

The two equations are solved simultaneously with the boundary conditions mimicking the physical problem being addressed. Fluid at the entrance is considered to enter as a free stream and follows the no-slip boundary condition at the wall. The CNPs and plasma proteins are assumed to be dispersed homogeneously in the solution at the entrance at their respective concentrations and follow no-penetration boundary condition at the wall. The flow domain is discretized in triangular elements and the grid size was reduced until there was a less than 2% difference in the simulation results. The convergence criterion was set specifying the tolerance level at 10^{-6}, for the relative error based on preceding iteration value.

The numerical modelling results indicate that the mixing of the CNPs with plasma proteins takes place instantaneously. Even before it reaches the first bend, the solutions are thoroughly mixed. This proves that the design of the microfluidic channel is conducive for on-chip plasma protein adsorption on nanoparticles. COMSOL generated image for fluid velocity in the entire microfluidic device with both plasma proteins and CNPs incubation are shown in Figure S11 in the Supporting Information.

2.3. Microfluidic Technology Enabled Dynamic Protein Corona Monitoring

An integrated microfluidic system was devised and composed of an electrical impedance chip, microfluidic device, and bonded Au electrodes within a specific section of the microfluidic channels, which was used to monitor real-time protein corona complex formation under controlled flow conditions. The electrical impedance setup consisted of evaporated Au electrodes pads that which were connected to an impedance analyzer to record the base resistance and the change in resistance of the surrounding solution which was flowing through the microfluidic device. Scanning electron microscopy (SEM) images were collected at different locations of the microfluidic device, including the channels and gold electrodes (Figure S12, Supporting Information) to demonstrate successful fabrication. As the voltage applied was of high frequency, hence impedance collected was taken approximately equal to resistance.

According to Onsager–Manning–Oosawa condensation,[45] charged colloids including CNPs also release counterions which are either free in the solution or adsorbed on their nanoscale surface. However, on close inspection of the change in resistance values for individual CNPs or plasma protein solution, it was evident that the latter are majority of the charge carriers thereby contributing toward the bulk of the electrical conductivity of the solution flowing through the microfluidic device (Figure S13a,b, Supporting Information). So, we hypothesize that initially, when only plasma proteins are flowing into the device, they readily produce their counterions and hence have high electrical conductivity (σ) of the solution or low change in electrical resistance (**Figure 3**a and Figure S13, Supporting Information). Upon addition of CNPs, it leads to adsorption of proteins onto the nanoscale surface of CNPs leading to the formation of protein corona complexes. However, the subsequent counterions being released due to the adsorption process gets confined within the protein corona complex and no longer freely available in the solution to account for the electrical conductivity of the solution. Consequently, this decrease in electrical conductivity leads to an increase in the change of electrical resistance of the solution flowing through the microfluidic device. At a later time point, say $t = 3$ or 6 h, proteins which were less abundant but had more affinity for the CNP, try to adsorb on their surface displacing an earlier bound relatively abundant protein. However, counterions of the recently displaced protein along with the newly adsorbed protein could still remain confined within the protein corona complex, thereby causing a massive depletion in the number of free counterions in the solution, leading to a much higher change in electrical resistance of the solution. We additionally performed electrical conductivity measurements (Figure 3b–e), the effect of dilution of plasma proteins on electrical resistance (Figure S13b, Supporting Information) along with monitoring the time-dependent change of electrical resistance measurements (**Figure 4**) of each CNP–protein corona complexes which confirmed our hypothesis. Diluting the plasma proteins solution (with phosphate bovine serum (PBS) 1× buffer) resulted in lowering the effective number of charge carriers (or counterions), thereby decreasing the overall electrical conductivity of the solution, or increasing the electrical resistance of the solution.

As a first step, three microfluidic devices embedded with Au microelectrodes (marked accordingly the locations in Figure S14, Supporting Information) were developed with similar dimensions and connected in series via tubing and were interfaced with a mechanical pump. Plasma proteins as referred throughout the work were lyophilized pooled human plasma.[46] Initially, CNPs (30 µL of 1 mg mL^{-1}) and plasma proteins (30 µL) were run at flow rate of 5 µL min^{-1} through separate inlets of the first microfluidic device at room temperature, followed by measuring of their individual resistance at each inlet just before they met at the junction for first mixing (Figure S14, Supporting Information). The second recording was captured immediately at $t = 10$ s at the junction of two fluids (CNPs and plasma proteins) with a flow rate of 0.2 µL min^{-1}. These recordings were used as a base reference to differentiate the mixture before and after corona formation. Following their initial mixing, plasma protein–CNP mixture
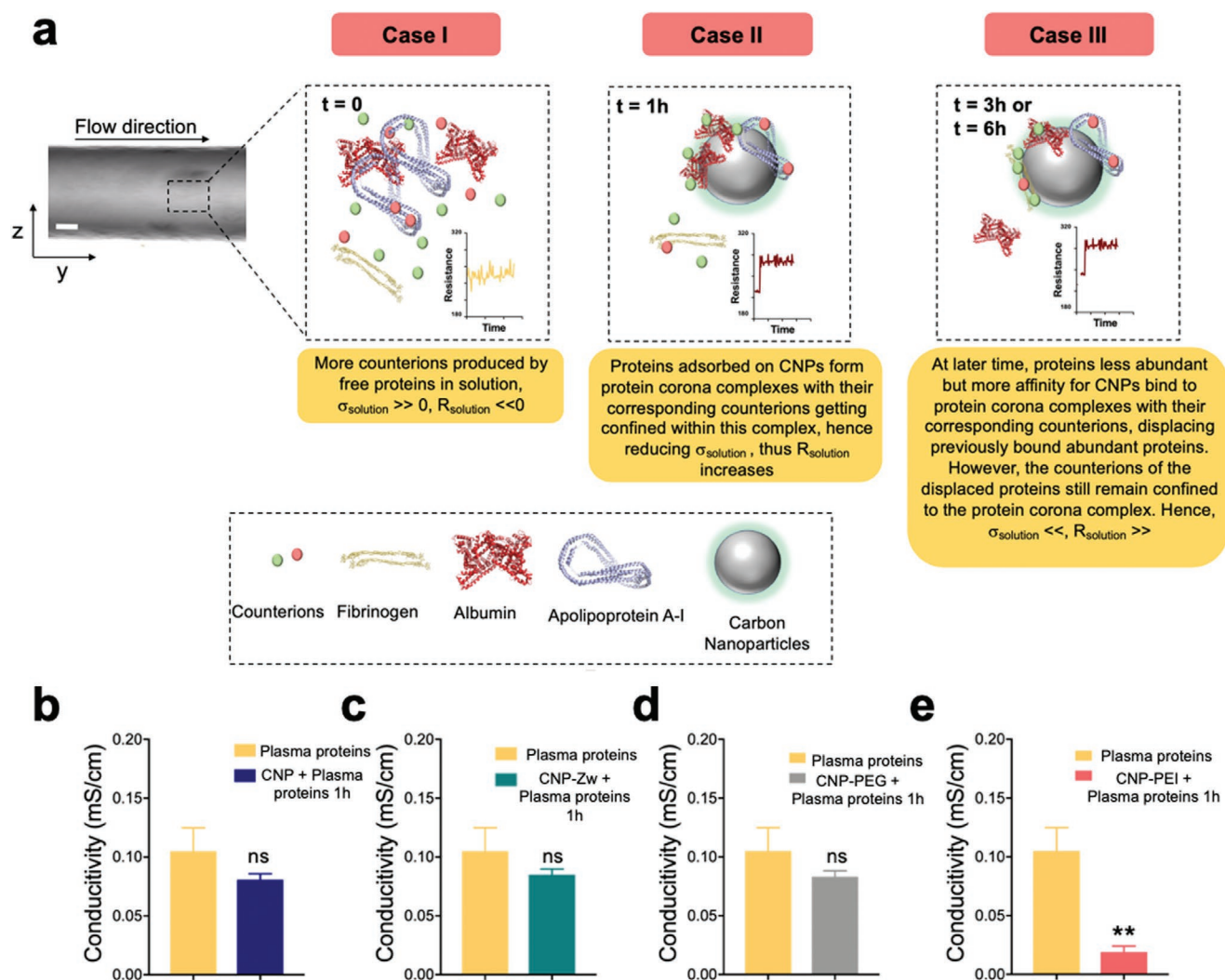
Figure 3. a) Schematic to demonstrate the electrical conductivity and free counterions approach utilized in this work. b–e) Electrical conductivity measurements were performed to validate the above model. Plasma proteins were initially showing a high electrical conductivity, however, upon subsequent incubation with the CNPs lead to a drop in its value. However, on close inspection, it revealed that CNP–PEI suffered the most drop in electrical conductivity compared to bare CNP, CNP–Zw or CNP PEG, probably due to its positive charge, allowing bulk of the negatively charged plasma proteins to adsorb on its surface and drastically reduce the charge carriers in the solution.

were incubated in serpentine channels for ≈1 h (also at flow rate of 0.2 µL min^{-1}), after which, with the help of syringe pump, they were pushed through the outlet at constant flow rate and consequently, electrical resistance was recorded for a period of 1 h. ≈60 µL was collected in a centrifuge tube and immediately frozen to stop the protein adsorption process. The samples collected in centrifuge tubes were further subjected to washing steps to remove the loosely bound or unbound proteins from the particles and resuspended in media. Different physiochemical characterizations studies such as DLS, zeta potential, and photoluminescence emission spectra along with SDS-PAGE gel were performed for all the collected samples. Each incubation experiments were performed on three separate days, under similar conditions and plotted as mean ± standard deviation in Figure 4a. For performing incubation experiments at higher times (i.e., 3 and 6 h), same experiment setup was used but

rather than storing the sample in centrifuge tubes at the end of 1 h, the entire sample was then sent to second microfluidic device (B) via tubing for further incubation in the serpentine channels for 2 h (again at low flow rate), followed by electrical resistance recording from $t = 3$ to 4 h or 6 to 7 h, and collection of samples in centrifuge tube eventually.

From the resistance profile of different CNP–plasma protein mixture, it was observed that for CNP–PEI, with an increase in time, the electrical resistance increased the most, going from 238 ± 16 Ω at $t = 0–1$ h to 301 ± 14 Ω for $t = 3–4$ h to finally 326 ± 14 Ω for $t = 6–7$ h. According to our hypothesis, increased electrical resistance should be associated with a drop-in electrical conductivity of the solution due to a decrease in charge carriers in the systems since the positively charged CNP–PEI attracts a majority of the negatively charged plasma proteins through columbic attractions and forms a hard
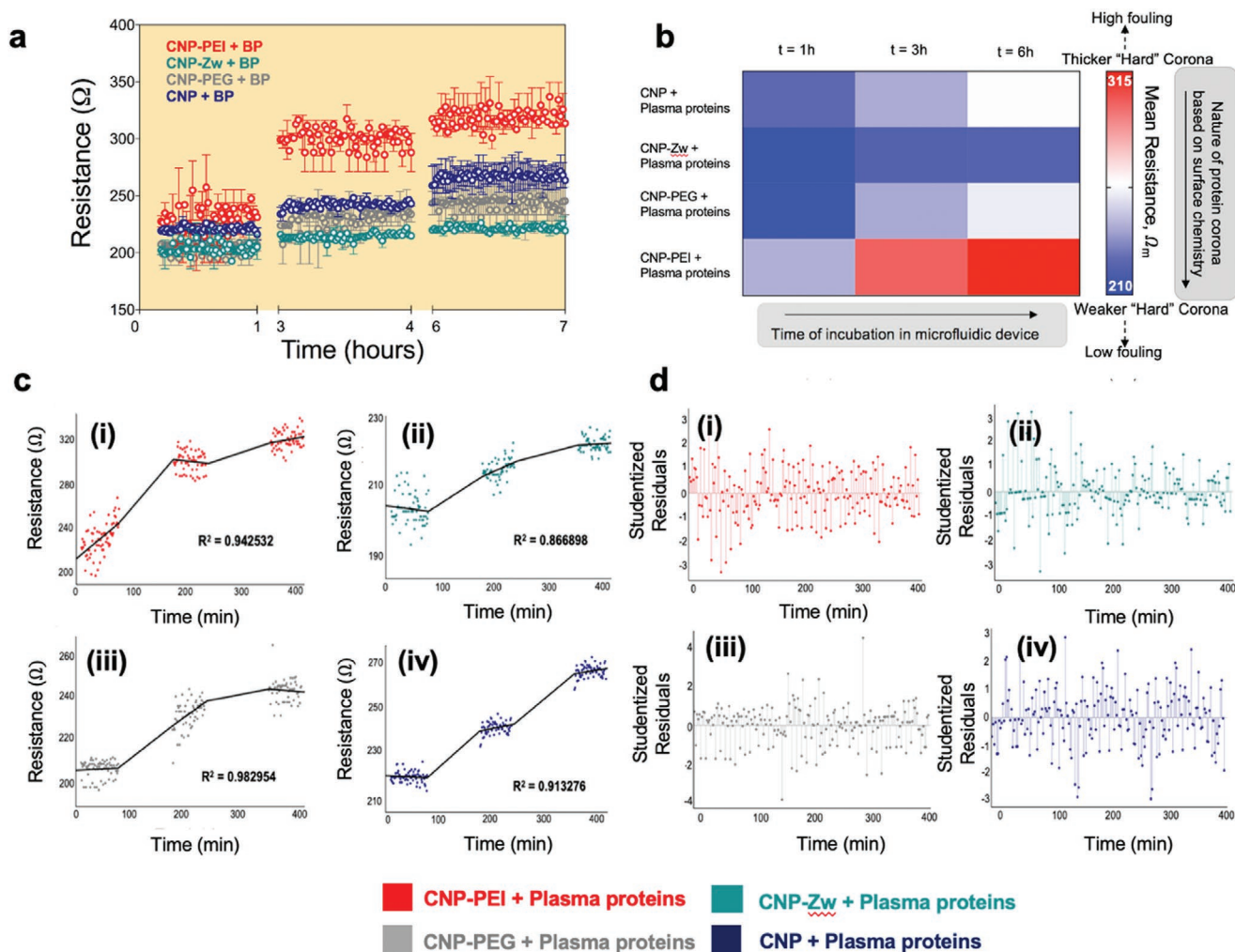
**ADVANCED
SCIENCE NEWS**

www.advancedsciencenews.com

**small
methods**

www.small-methods.com

Figure 4. a) Electrical resistance collected in a real-time manner for CNPs (having different surface chemistries) and plasma proteins via the gold electrodes fabricated on the microfluidic device. Two more microfluidic devices were connected in parallel via tubing to obtain electrical resistance measurements for higher incubation time ($t = 3$ and 6 h) as shown in Figure S14 in the Supporting Information. b) A preliminary heat-map analysis was performed to simplify and generalize the results obtained from our integrated microfluidic platform. Electrical resistance values obtained at $t = 1$, 3, and 6 h for each NP and plasma proteins mixture were calculated and subsequently given a blue color if it had a low mean electrical resistance value, red color if it had a high mean electrical resistance value and white color if it was having an intermediate electrical resistance value (values obtained from (a)). Thus, having a red color on the heat map corresponds to an eventual formation of a stronger "hard" corona as was observed for CNP–PEI due to its cationic surface charge, indicating high fouling behavior. However, blue color indicates the formation of weaker "hard" corona was observed for CNP–PEG and CNP–Zw, owing to their low fouling properties. c) The B-spline fits performed using Mathematica are shown as a black line, and they correspond to i) CNP–PEI + plasma proteins, ii) CNP–Zw + plasma proteins, iii) CNP–PEG + plasma proteins, and iv) CNP + plasma proteins, respectively. The adjusted R^2, a widely used goodness of fit measure, is shown in the figure. d) The studentized residuals, which correspond to the quotient of the division of the residual by the estimate of the standard deviation is also shown and each correspond to CNP–PEI + plasma proteins (red, i), CNP–Zw + plasma proteins (green, ii), CNP–PEG + plasma proteins (gray, iii) and CNP + plasma proteins, respectively (blue, iv).

corona. CNPs having a surface coating of PEG (CNP–PEG) or zwitterionic lipids (CNP–Zw) did not show any appreciable change in electrical resistance with increased incubation time (Figure 4a, Figure S15, Supporting Information). This could be attributed to the fact that having a PEGylated or lipid wrapping on CNPs imparted them with better stealth properties and did not allow majority of the proteins to be adsorbed on the nanoparticles surface unlike a PEI wrapping.[47–49] A preliminary heat-map analysis was also performed to simplify and generalize the results obtained from our integrated microfluidic

platform. Electrical resistance values obtained at $t = 1$, 3, and 6 h for each NP and plasma proteins mixture were calculated and subsequently, color-coded with a blue color if it had a low mean electrical resistance value ($R \approx 210\ \Omega$), red color if it had a high mean electrical resistance value ($R \approx 315\ \Omega$ and white color if it was having an intermediate electrical resistance value (Figure 4b). Thus, as the incubation time increased gradually from 1 to 6 h, we noticed that CNP–PEI due to its cationic charge eventually formed a relatively thicker "hard" corona evident from the heat map showing an increase in

**ADVANCED
SCIENCE NEWS**

www.advancedsciencenews.com

**small
methods**

www.small-methods.com

mean resistance value (with color in heat map changing from light blue to dark red via light red) possibly indicating high fouling behavior. However, for CNP–PEG and CNP–Zw, due to their low fouling characteristics, they did not exhibit any drastic increase in mean resistance values, as also evident from the heat map.

2.4. Statistical Analysis of Microfluidic Resistance Data

After collecting the resistance data from our integrated microfluidic setup, we attempted to do a curve fitting or regression analysis which involved approximating the data points with a curve defined by some mathematical function and subjecting it to constraints. This ensures that we can possibly draw an inference of the values of the resistance for times where we have not collected the data. Since the data we collected demonstrated natural break points (due to incubation period in the microfluidic device, and hence no data being collected), instead of fitting a higher degree polynomial for the entire range of data, we used a spline function composed of a sum of B-splines for fitting using a method of least squares (linear model fitting). Since there was no theoretical basis for choosing one fitting function over another, we chose the above method. The objective function used here for the least square minimization is, for a spline function of degree k

$$U = \sum_{\text{all } x} \left\{ W(x) \left[\gamma(x) - \sum_i \alpha_i \beta_{i,k,t}(x) \right] \right\}^2 \qquad (5)$$

where $W(x)$ is a weight and $\gamma(x)$ is the datum value at x. The knot values may be fixed, or they can also be treated as parameters. The knot values in this case were easily determined, because of the prior knowledge of data generation and the time intervals at which the data was generated. The degree of freedom for the spline functions was kept at a minimum to avoid overfitting. [50]

The resistance data points collected from our integrated microfluidic setup shown in Figure 4c, corresponding to CNP–PEI + plasma proteins, CNP–Zw + plasma proteins, CNP–PEG + plasma proteins and CNP + plasma proteins, refer to the average values of two readings, for all these four different NP–plasma protein combinations. The B-spline fitting was performed using Mathematica.[51] The fitted splines are shown in black and the knots for the spline fits are inferred from the previous knowledge of data generation and they correspond to 0, 80, 180, 245, 360, and 425, respectively. The degree of the fit was kept at 1, to avoid potential overfitting. The model was automatically fitted using the LinearModelFit function of the software, the list of models compared can be provided upon request. We calculated the R^2 values, which were close to one, further demonstrating that the data are closer to the fitted regression line.

For a quantitative estimation of the goodness of fit, we also plotted the studentized residual (which corresponds to the quotient of the division of the residual by the estimate of the standard deviation) in Figure 4d for all the four different NP–plasma protein combinations. The residuals did not show any underlying pattern and seemed to be distributed randomly following a normal distribution. We further calculated

the Adjusted R^2, Akaike Information Criteria (AIC), Bayesian Information Criteria (BIC), and Akaike Information Criteria corrected (AICc) values, statistics used to measure the goodness of fit of a model. While R^2 is proportional to the variance of the parameters, Adjusted R^2 is a modified version of R-squared that has been adjusted for the number of predictors in the model and values closer to 1 indicate perfect fit (Tables S2 and S3, Supporting Information). The parameters AIC, BIC, and AICc are all related to maximizing the likelihood function and penalizing the increase in the number of parameters. Maximizing the likelihood function rewards the goodness of fit, while penalizing the number of parameters discourages overfitting. Lower values of AIC, BIC, and AICc are used for model selection.

2.5. Utilizing Wavelet Transforms to Study "Soft" and "Hard" Protein Corona Formation

Resistance change over time (alternatively referred to as time-series signal) as collected via our integrated microfluidic setup, provided comprehensive information about the signal characteristic in the time domain. However, frequency information cannot be gathered in this current form. Although the Fourier transform of the time-series signal can provide a full insight into the frequency information of the time-series signal, however, no time information would be available. Neither the signal in the time domain nor the Fourier transform of the signal in the frequency domain provides a full description of the signal. Hence, in this work, WT has been utilized for the analysis of the resistance-time signal in the time-frequency domain.[52] Wavelet analysis is a powerful time-frequency analysis tool garnered great attention in biology recently,[53] which is based on decomposing the signal into a set of wavelets functions.

The wavelet transforms, $\varnothing_{jk}(t)$ is based on decomposing the signal using orthogonal wavelet as shown in the following equation which represents the wavelet series

$$x(t) = \sum_{j,k=-\infty}^{\infty} B_{jk} \varnothing_{jk}(t) \qquad (6)$$

The WT of a signal $x(t)$ is defined as

$$\text{CWT}(a,b) = \int x(t)\,\psi_{a,b}(t)\,dt \qquad (7)$$

where

$$\psi_{a,b}(t) = \frac{1}{\sqrt{|a|}}\,\psi\!\left(\frac{t-b}{a}\right) \qquad (8)$$

ψ is known as the mother wavelet and $\psi_{a,b}(t)$ is the dilation and transformation of ψ, "b" is a time shifting parameter that captures the time domain information of the signal $x(t)$. "a" is a scaling parameter, which provides the mother wavelet function $\psi(s)$ dilation and compression characteristics. By utilizing this technique, a scalogram of each time-series signal can be generated which represents the absolute value of the wavelet transform output, as a function of time and frequency. Therefore, wavelet analysis used to resolve the frequency content of the

**ADVANCED
SCIENCE NEWS**

www.advancedsciencenews.com

**small
methods**

www.small-methods.com

signal at each time point. Hence, we feel that would let us get valuable information about the dynamics of protein adsorption and desorption events onto the surface of CNPs with varied surface chemistry from the frequency point of view with a high temporal resolution.

During the protein corona formation, there is competition among innumerous plasma proteins to adsorb onto the NP surface, a phenomenon that has been well studied by researchers. From the thermodynamic point of view, the "hard" corona adsorbs onto the surface of NPs in a thermodynamically favorable manner with a large net binding energy of adsorption (ΔG_{ads}), which determines the stability of the NP–protein complex. Consequently, proteins that adsorb with a large ΔG_{ads} have a low probability of desorption and tend to stay associated with the NPs. On the other hand, proteins that adsorb with small ΔG_{ads} can easily desorb and return into the solution, as is the case with "soft" corona. Cedervall et al.[14] conducted a study where they modeled the total plasma protein adsorption using a biexponential function which allowed them to divide protein adsorption and desorption events into "fast" and "slow" components, respectively having their own "effective" k_{on} and k_{off} values. Considering these fast and slow components of adsorption and desorption presumably refers to the hard and soft coronas, according to some recent literature reports. However, the soft and hard corona are alternatively indicated with the terms of the "fast component" and "soft" component when referring to the desorption process.[54–56]

Hence, we attempted to utilize this information efficiently interpreting our wavelet transform data. The real-time resistance data collected from our integrated setup was converted into wavelet scalograms for both CNP–PEI 1 h and CNP–Zw 1 h. After this, we divided the wavelet scalogram for both into two halves/regions, i.e., high frequency region (top half, $v1$) and low-frequency region (bottom half, $v2$), from which we collected two spectra which averaged the frequency spectra over time for both halves. A "hard" corona which gets formed when proteins bind to NPs with a large ΔG_{ads}, have slower exchange rates between NPs and proteins, corresponding to a lower rate of frequency change and hence was classified in low frequency region, $v2$. Likewise, "soft" corona would have much higher exchange rates between NPs surface and proteins due to a lower small ΔG_{ads} so they can easily desorb and return into the solution, we believed that it would correspond to the higher frequency region (**Figure 5**a). By comparing the plots of hard corona (or $v2$) for CNP–PEI 1 h and CNP–Zw 1 h and comparing their maximum magnitudes at $t \approx 20$ min, we observed that it was fourfold higher for the former, possibly indicating a formation of thicker corona due to the abundance of cationic functionalities Figure 5b,c.

Furthermore, Figure 5d,e shows the scalograms for CNP–PEI and CNP–Zw (at all time points, i.e., 1, 3, and 6 h) and by selecting a particularly high frequency point (which could correspond to the "soft" corona as explained earlier) depicted a higher degree of exchange occurring between CNP–PEI and plasma proteins at $t = 1$ h which eventually drops in magnitude. However, by selecting a high frequency for the CNP–Zw, we noticed that the magnitude of exchange was much less, i.e., less than twofold when compared with CNP–PEI at ≈20 min of incubation of CNPs and plasma proteins. These results could possibly imply that CNP–PEI forms a thicker corona when compared to CNP–Zw.

Thus, WT analysis presents comprehensive insight and a quantitative indication about the dynamics of protein adsorption and desorption events occurring on the nanoparticle surface can be inferred from the resultant output. It is important to note that the experiments were carried out at a fixed flow rate, and hence, the protein adsorption–desorption dynamics obtained via WT analysis corresponded to that flow rate. A change in the flow rate could lead to different protein adsorption–desorption dynamics.

2.6. Prediction of Fouling Behavior of CNP–Protein Corona Complexes and Correlation with Thickness of "Hard" Corona Aided via Machine Learning (ML)

To make our integrated microfluidic setup more robust in efficiently differentiating fouling behavior of different surface passivation's on CNPs when they eventually formed protein corona complexes, we attempted to integrate the results with ML algorithms that would potentially be able to rapidly classify it as "low," "high," or "intermediate" fouling categories (as fast as ≈1 h). We envision that this will eventually be able to extend across different nanoparticle platforms. For developing the ML model for estimation of the fouling behavior, we first calculated the Shannon entropy from the resistance values obtained over-times from the integrated microfluidic setup. These entropy values provide us information about the complexity of the change in resistance which could reflect the dynamics of the protein adsorption events at the NP surface.

Shannon entropy was calculated based on the following equation

$$E = -\sum P_i \log_b P_i \tag{9}$$

where P_i is the probability of a value i showing up in a stream of data.

Shannon entropy was combined with the maximum energy obtained from WT applied on the time-series signal as described in the previous section and fed into the ML model. These data were clustered in a user-blinded study using k-means clustering, a powerful unsupervised ML algorithm which is often using in pattern recognition.[57,58] The commonalities in the dataset extracted from monitoring the change of solution impedance/resistance which would reflect the dynamics of protein adsorption on the NP surface and could identify and cluster by ML accordingly. Each of the four CNPs explored in this study were well-clustered into three types of fouling behavior and discriminated completely from each other with nearly 100% accuracy. (Figure 5f)

As seen in Figure 5g, the distribution of the three types of protein corona in the 2D feature space associated with their categories, where the high fouling behavior could lead to a more thicker layer of "hard" corona was placed toward the right, low fouling behavior corresponding to a thinner "hard" corona was on the left bottom, and the intermediate fouling behavior was placed in the middle. The 100% accuracy of the corona discrimination was achieved and proved by unsupervised clustering, demonstrating that combining ML makes it more robust and effective in classifying the fouling behavior of different CNP–protein corona complexes as low fouling, high fouling and
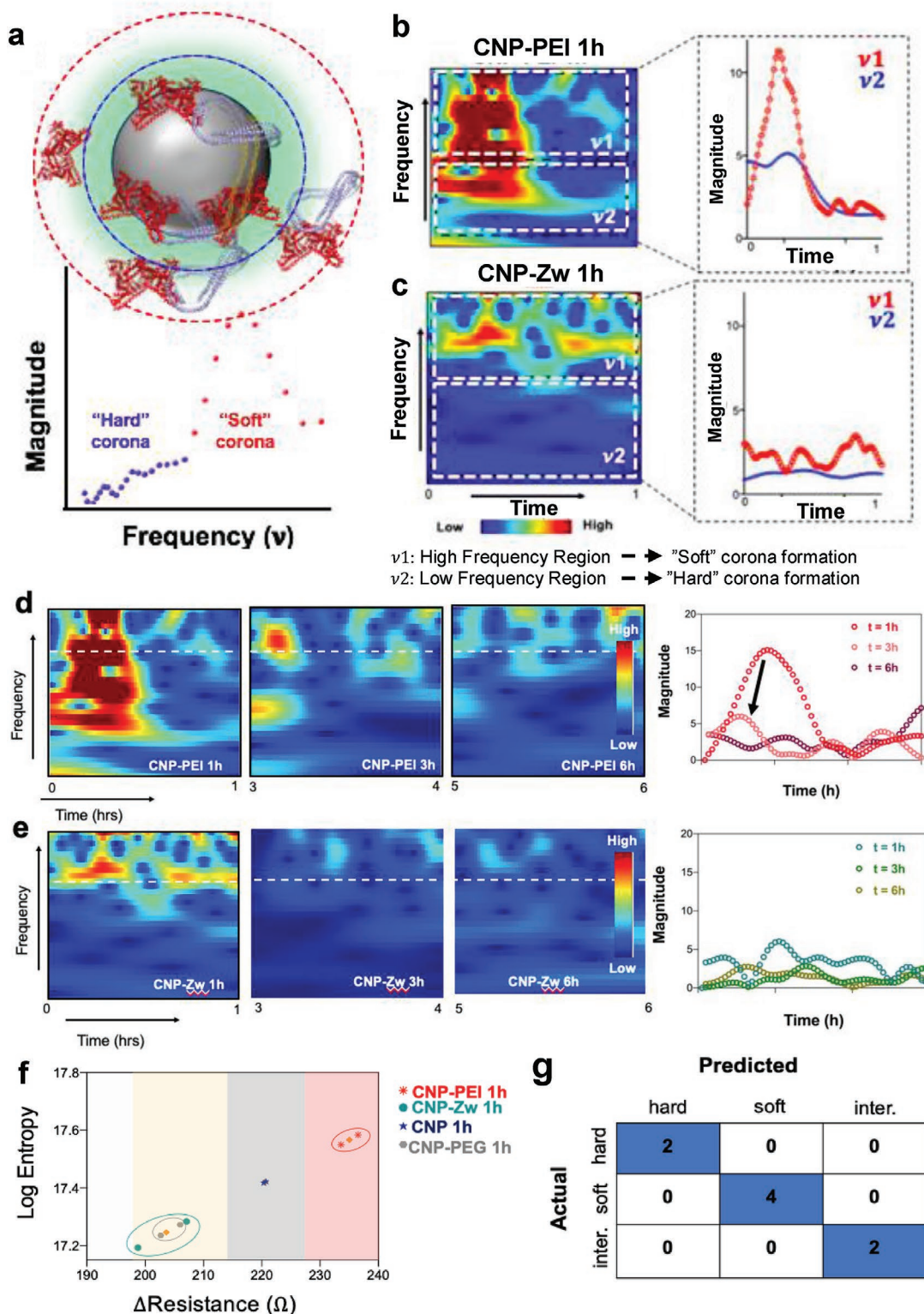
Figure 5. a) Schematic representation the hard (blue circle) and soft (red circle) corona regions on CNPs and their correlation with the frequency change. b,c) Wavelet scalograms of CNP–PEI 1 h and CNP–Zw 1 h, where the wavelength coefficients are plotted against time as a result of signal project on wavelet basis using the Morlet continuous time wavelet transform (CWT) with the color scale is represented in octave. The wavelet scalograms for each were divided into two halves, comprising of high frequency and low frequency events by averaging the frequency spectra over time for both halves. d,e) Spatial position plotted against time in an illustrative dashed line trajectory in hard and soft corona scalogram, respectively. The plots highlight the pattern of protein adsorption at preselected resistance rate (mHz) as a function of time, which indicate the dynamic of protein corona formation as a matter of time. f) The 2D space distribution of the ML input features and the corresponding clusters. The centroid of each cluster was depicted in orange. g) The matching matrix of the unsupervised ML model.
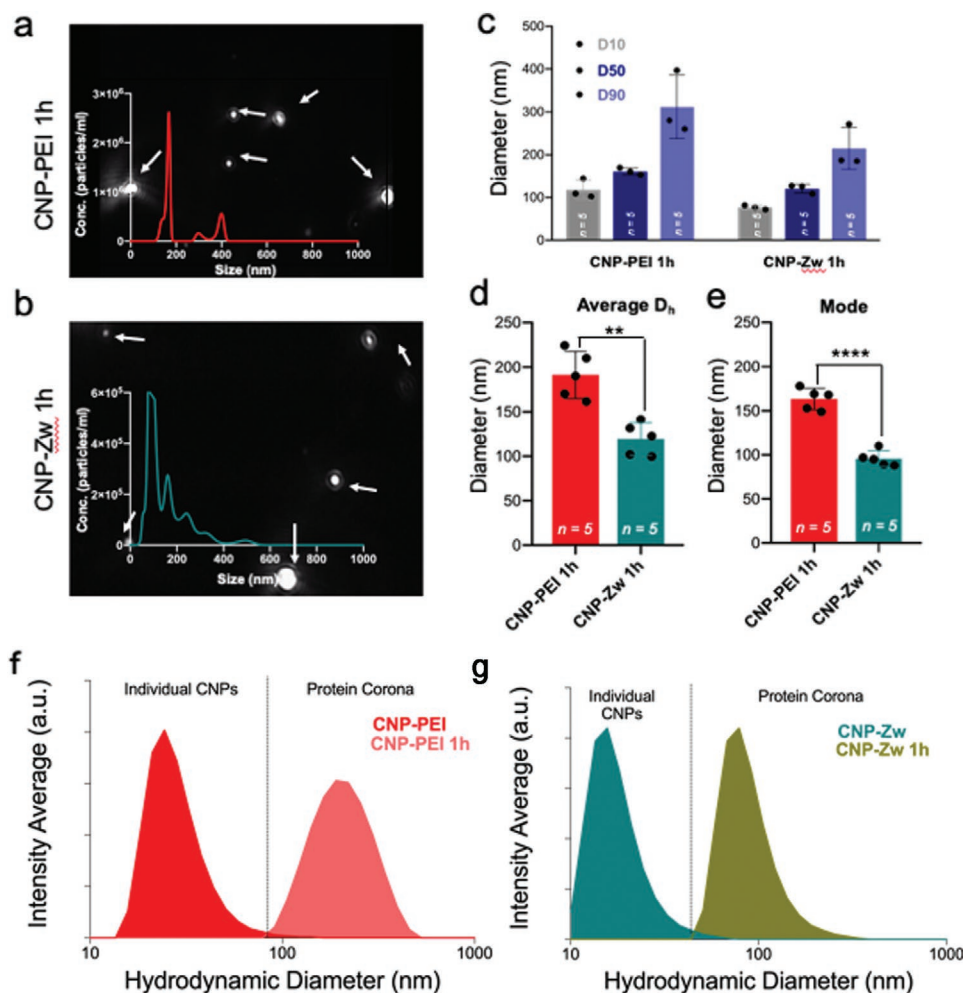
**ADVANCED
SCIENCE NEWS**

www.advancedsciencenews.com

**small
methods**

www.small-methods.com

Figure 6. Hydrodynamic diameter measurements of CNP–protein corona complexes from NTA. a,b) Screenshots from videos collected by Nanosight for size analysis of CNP–PEI 1 h and CNP–Zw 1 h with white arrows pointing to some examples of nanoparticles and the overlays depicting representative nanoparticle size distributions (concentration versus size). c) Hydrodynamic size distribution was evaluated with 10% of the detected CNP–protein corona complexes have sizes below D10, 50% of detected CNP–protein corona complexes have sizes below D50 and 90% of detected CNP–protein corona complexes have sizes below D90. d) Average hydrodynamic diameter for CNP–PEI 1 h and CNP–Zw 1 h. e) Mode hydrodynamic size, i.e., size with the highest frequency of occurrence were collected for both CNP–PEI 1 h and CNP–Zw 1 h. f,g) Hydrodynamic diameter measurements from DLS for CNP–PEI and CNP–Zw before and after protein corona formation.

intermediate fouling even at ≈1 h. The unsupervised ML classified the data based on Euclidean distances which are used to compute point-to-cluster-centroid distances of the three classification groups based on the two-input features. The data points were clustered into groups based in the shortest Euclidean distance value from the cluster of the centroid. Based on the eight unknown samples (four different CNPs and microfluidic experiment carried out on two separate days) were completely identified with a detection accuracy of 100% in user-blinded study, demonstrating the efficiency of the proposed approach.

2.7. Physicochemical Characterization of Protein Corona–CNP Complexes

At the end of the incubation period, samples were collected from the designated outlets and several physiochemical characterization studies including measuring their hydrodynamic diameter

measurements (both via DLS and nanoparticle tracking analysis, i.e., nanoparticle tracking analysis (NTA)), zeta-potential measurements, and fluorescence excitation–emission studies were conducted to understand the protein corona complex thus formed.

Hydrodynamic diameter measurements along with size distributions were first determined by NTA which recorded five 1 min videos for both CNP–PEI 1 h and CNP–Zw 1 h. (**Figure 6**a,b) D10, D50, and D90 values were recorded which indicated that on average 10% of CNP–protein corona complex were less than 105 nm for CNP–PEI 1 h and 80 nm for CNP–Zw 1 h, 50% are below 150 nm for CNP–PEI 1 h and 110 nm for CNP–Zw 1 h, and 90% are below 305 nm for CNP–PEI 1 h and 200 nm for CNP–Zw 1 h (Figure 6c). The average hydrodynamic size for CNP–PEI 1 h and CNP–Zw 1 h was found equal to ≈195 and 105 nm, respectively (Figure 6d). The mode size was also selected across all the five videos and found to be around 160 nm for CNP–PEI 1 h and 95 nm for CNP–Zw 1 h
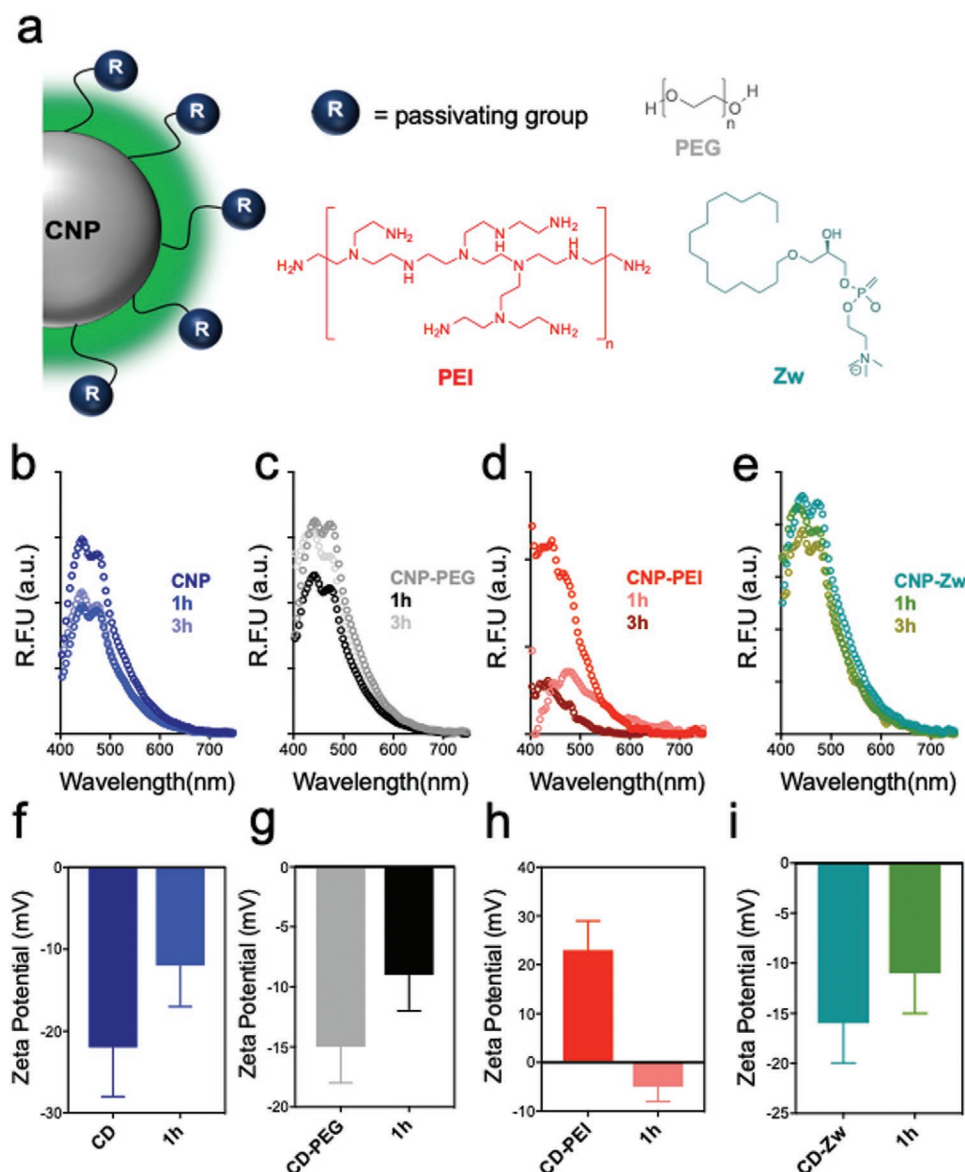
Figure 7. a) Bare CNPs (no passivation) and CNPs functionalized with zwitterionic (Zw), polyethyleneimine (PEI) and polyethylene glycol (PEG) functionalities were used in this study. The effect of the protein corona formation on the physiochemical properties of CNPs were investigated by b–e) fluorescence intensity measurements at 365 nm excitation wavelength and f–i) ζ-potential distributions, before and after (1 h) protein corona complex formation.

(Figure 6e). DLS studies revealed a significant increase in the hydrodynamic diameter for CNP–PEI from 40 to ≈220 nm after incubating it with plasma proteins (Figure 6f,g). It is probably attributed to its cationic surface, which owing to columbic interactions attract most of the plasma proteins which are negatively charged, thereby forming an extended protein–CNP complex along with a possibility of protein corona mediated CNP aggregation. Both NTA and DLS measurement techniques complemented well with each other by similar hydrodynamic diameter values for the CNP–protein corona complexes formed, i.e., CNP–PEI 1 h and CNP–Zw 1 h.

Excitation–emission studies performed revealed a drop-in fluorescence emission for anionic and cationic CNPs once the protein corona was formed (**Figure 7**a–e). We also performed

additional calculations to show the percentage drop in fluorescence intensity for different CNPs after 1 and 3 h of incubation (Figure S16, Supporting Information). However, the decrease in emission intensity was minimal for neutral and zwitterion CNPs in comparison with CNP or CNP–PEI. This behavior is attributed to the antifouling behavior of PEGylated and zwitterionic surface functionalities which prevent plasma proteins to adsorb readily on the nanoparticle surface, as described elsewhere. [47–49] Interestingly, the emission peak of CNP–PEI red shifts after 1 h of incubation with plasma proteins, and blue shifts at the end of 3 h. A plausible reason for such an observation could be that CNP–PEI due to its cationic charge adsorbs bulk of plasma proteins leading to a formation of a thicker "hard" corona resulting in redshift in fluorescence
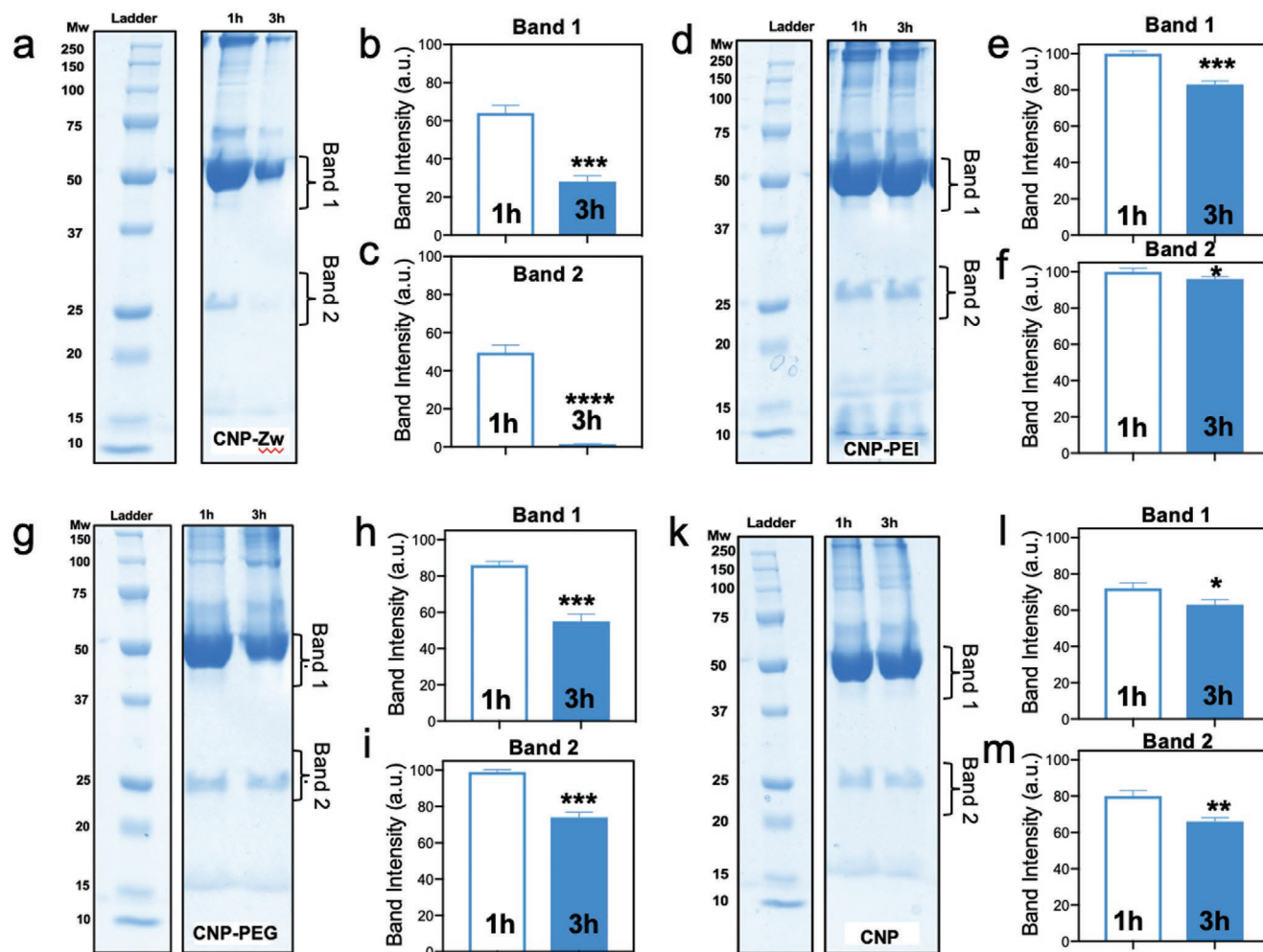
ADVANCED
SCIENCE NEWS
www.advancedsciencenews.com

small
methods
www.small-methods.com

Figure 8. SDS-PAGE gel analysis after incubating the CNPs with plasma proteins in the microfluidic setup for different times (1, 3 h). a,d,g,j) Coomassie stained gel lanes for bare CNP, CNP–PEG, CNP—Zw, and CNP—PEI, respectively obtained at the end of the incubation in the microfluidic device for 1 and 3 h. Each type of CNP gel is represented by the molecular weight lane marked as ladder. Corresponding regions highlighted as Band 1 and Band 2 were analyzed using ImageJ for each CNP type with incubation time of 1 and 3 h and normalized band intensities were plotted as shown in (b,c,e,f,h,i,l,m).

emission. However, since the protein corona complex for CNP–PEI is dynamically changing as evident from our WT studies in Figure 5d. the "hard" corona changes in composition and becomes relatively thinner and leads to blueshift in fluorescence emission. Further experiments are needed to validate this effect, which is currently out of the scope of this work. Zeta potential measurements were further taken into consideration to study protein corona. The initially cationic CNP–PEI ($\zeta = +24$ mV) became anionic ($\zeta = -9$ mV) following the corona formation. It can be seen in Figure 7f–i that the anionic CNPs, neutral CNPs, and zwitterion CNPs have negative zeta potential but shown an increased value once the corona has been formed in any individual case, thereby reflecting the charges of the adsorbed proteins. These results further confirms that despite of plasma proteins have a net negative charge, they have regions of positive and negative charge which allows the proteins to form complexes with charged CNPs as shown in previous works. [59,60] We further performed intensity averaged hydrodynamic diameter measurements as well as zeta potential measurements for all

CNPs at $t = 0$ and 1 week to confirm their stability (Figures S9 and S10 and Table S4, Supporting Information).

2.8. Investigation of Plasma Protein–CNP Complexes via SDS-PAGE and Liquid Chromatography-Mass Spectrometry (LC-MS) Analysis

Once we had analyzed the real-time formation of the protein corona formation using our microfluidic setup followed by distinguishing "soft" or "hard" protein corona processes using WT and ML tools as well as preliminary physiochemical characterizations, we attempted to qualitatively and semi-quantitatively analyze the protein adsorption profiles for all the CNPs. Prior to performing a comprehensive proteomics analysis of the protein corona complexes formed by respective CNPs, the molecular composition of the adsorbed plasma proteins was measured by denaturing SDS-PAGE Coomassie stained gel lanes as shown in **Figure** 8a–l. The highlighted

portions in the bands marked as "Region 1" and "Region 2" were the regions which were analyzed using ImageJ to calculate the optical intensity.[61–63] Plasma proteins alone (without any CNPs) were subjected to identical washing steps (i.e., centrifugation at 25 000 rpm, followed by washing with PBS several times) similar to that of CNP/protein complexes (Figure S17, Supporting Information). The intensities of the bands obtained for these in Band 1 and Band 2 were classified as background and subtracted from each of the Band 1 and Band 2 obtained for CNP/protein complexes. The band intensities for Band 1 and Band 2 were also normalized across all samples. Corresponding profiles generated revealed a drop of band intensity at incubation for 3 h compared to incubation for 1 h for almost all protein–CNP complexes, revealing the dynamic nature of corona formation which were consistent across different days of performing the microfluidic experiments, followed by running SDS-PAGE gels. Hence for plotting the band intensities for Band 1 and Band 2 for different CNP/protein complex (Figure 8b,c,e,f,h,i,l,m), the average intensities from each day were considered. On closer inspection, it was observed that having a zwitterionic or PEGylated surface coating could lead to a reduction in interaction with plasma proteins at higher incubation time (i.e., 3 h). However, having a cationic surface coating (CNP–PEI) did not lead to any noticeable drop in band intensity for either regions, thereby indicating a continued interaction between the mostly negative plasma proteins and cationic CNP–PEI. This further indicates a preferential interaction of different plasma proteins with the nanoscale surface based on their surface chemistry, ultimately leading to an increased local concentration around the nanoparticles, leading to a specific composition of the protein corona.

From LC-MS analysis, we attempted to understand the role of a specific surface functionality on the formation of the corona along with the incubation period, and further classify the proteins, according to their function in blood namely complement activation, immune response, coagulation, acute phase, lipoproteins, and tissue leakage. On further analysis, both coagulations proteins as well as immunoglobulins were the major protein types, comprising up to 60–70% of the total proteins that were found in the corona composition irrespective of the surface chemistry of CNPs (**Figure 9**a–h). It was interesting to note that all CNPs strongly interacted with immunoglobulins, which are highly abundant in the blood and plays an important role in immune response by promoting phagocytosis.[64] Furthermore, complement proteins were found to be present in all CNPs indicating that the complement system plays a crucial role in clearing of the CNPs from the systemic circulation via reticuloendothelial system.

"Tissue leakage" protein, vitronectin was found to be present in all CNPs irrespective of their surface chemistries and are often associated with many diseases.[65] Apolipoproteins are the class of proteins that are present in all CNPs (except CNP and CNP–PEI incubated with plasma proteins for 1 h). Apolipoproteins have been recognized as an important class of proteins which dictate both in vitro and in vivo fate of the NPs. Interestingly, clusterin, which is a lipoprotein, was found to be the major protein present in the corona of PEGylated and lipid coated zwitterionic CNPs. It has been hypothesized that

clusterin adhesion onto the surface of both PEGylated CNPs and lipid-based zwitterionic CNPs induces a stealth effect and further inhibits nanoparticle uptake via phagocytes. These results further agree with earlier works that hydrophilic coating, e.g., PEG or lipids impart steric stabilization and consequently reduce surface adhesion of plasma proteins and thereby may prolong circulation half-lives in vivo.

Additionally, we attempted to inspect how the percentage of the total number of proteins adsorbed on each CNP–protein corona complexes at the end of either 1 or 3 h correlated with their nanoscale surface chemistry. We observed CNP–PEI had the most adsorbed proteins for both 1 and 3 h among all other CNPs utilized in this study (Figure S18, Supporting Information). As expected, CNP–PEG and CNP–Zw showed the least amount of total proteins adsorbed at 1 h which gradually decreased at 3 h.

We also attempted to quantify the detected proteins in the LC-MS study for different CNP–plasma proteins complexes using an existing method called as exponentially modified Protein Abundance Index (emPAI) protocol that offers approximate, label-free, relative quantification of proteins in a mixture based on protein coverage by the peptide matches in a database search result.[66,67] Classification of the surface bound proteins for different CNP–plasma protein complexes were performed both based on their molecular weights as well as in accordance with their physiological functions (Figures S19 and S20, Supporting Information).

3. Conclusion

We have presented a simple, inexpensive tool that may provide valuable information on how exposure to nanoparticles affects the biological responses of cells and organisms at "point-of-use." Our dynamic setup consists of an integrated microfluidic platform coupled with electrical resistance measurement setup to monitor the real-time formation of a biomolecular corona of CNPs having different surface charges (such as anionic, cationic, neutral, and zwitterionic) in a time-resolved manner. A distinct advantage of using such an approach over conventional in situ measurements is the ability to create a dynamic environment with precise control over fluid flow allowing shear force being imposed on NPs and proteins resulting in their rigorous mixing thereby simulating a realistic biological milieu. Furthermore, the integrated microfluidic/resistance setup effectively discriminated "soft" versus "hard" corona formation based on nanoscale surface chemistries when coupled with WT and ML tools, thereby potentially being able to classify the corona type more rapidly (as fast as ≈1 h) and eventually be able to extend across different nanoparticle platforms. According to our hypothesis, where an increase in electrical resistance should be associated with a drop in electrical conductivity of the solution due to a decrease in effect charge carriers in the system. Hence, positively charged CNP–PEI would attract a majority of the negatively charge plasma proteins through columbic attractions and formed a stronger and possibly thicker "hard" corona entrapping bulk of free counterions, decreasing the electrical conductivity and in turn making the change in electrical resistance high resistance as obtained from our integrated
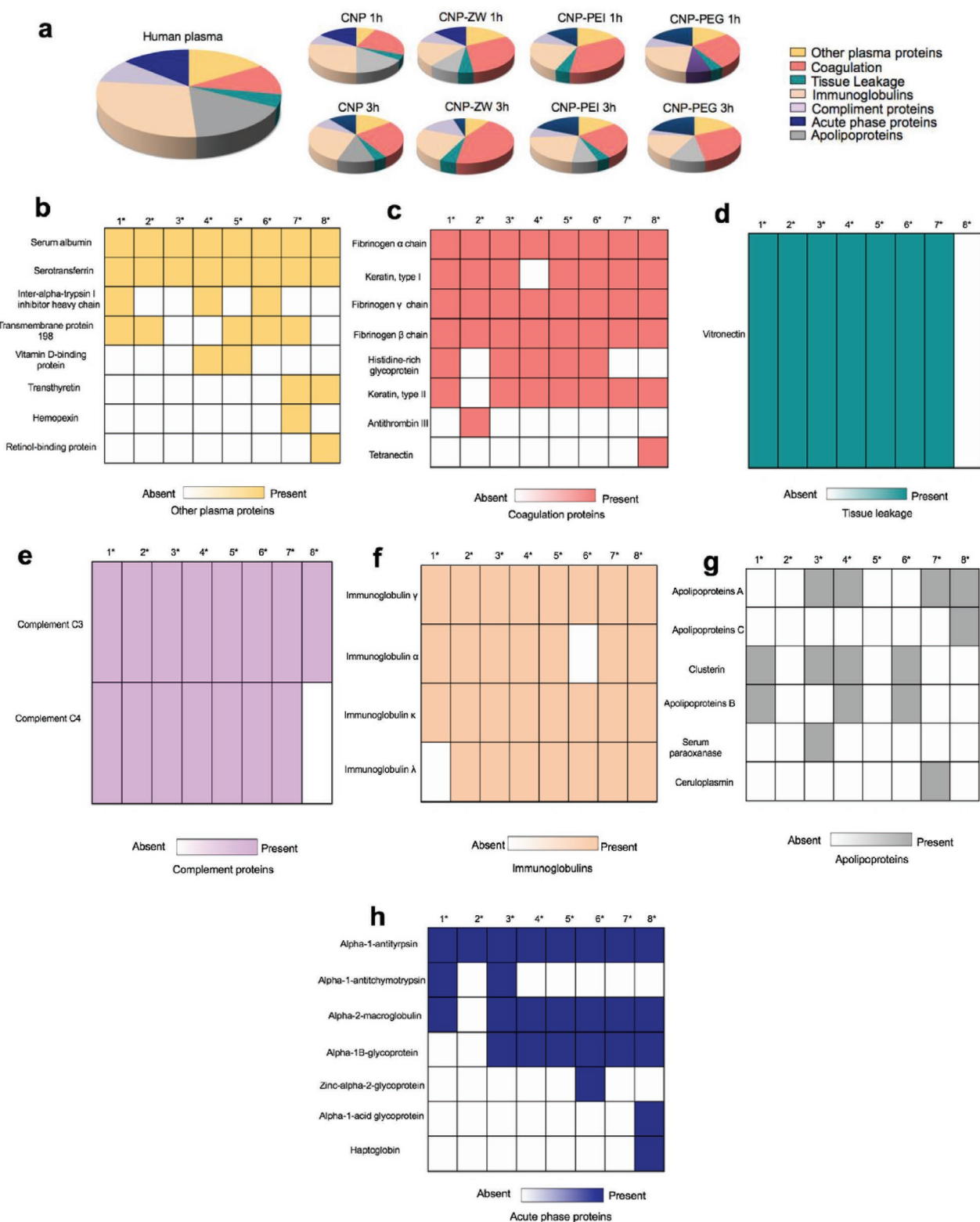
Figure 9. Proteomic analysis of the protein corona on the surface of different CNPs based on their functionality. a) Classification of protein corona components identified by quantitative LC-MS for each CNP type incubated in the microfluidic device for 1 and 3 h. A score of 50 or above was considered as significant, as obtained from LC-MS results and all the proteins above this score were further categorized according to relative abundances as well as their physiological functions such as b) other plasma proteins, c) coagulation proteins, d) tissue leakage proteins, e) complement proteins, f) immunoglobulins, g) apolipoproteins, and h) acute phase proteins and placed into heat maps as shown. 1′: CNP 1 h, 2′: CNP 3 h, 3′: CNP–Zw 1 h, 4′: CNP–Zw 3 h, 5′: CNP–PEI 1 h, 6′: CNP–PEI 3 h, 7′: CNP–PEG 1 h, 8′: CNP–PEG 3 h.

microfluidic setup. Contrastingly (Unlike CNP–PEI), both CNP–PEG and CNP–Zw did not express a significant change in the electrical resistance with increased incubation time inside the microfluidic channels. This could be attributed to the fact that having a PEGylated or lipid coating imparted the CNPs with well-known stealth properties and do not allow the majority of the proteins to be adsorbed on the NPs surface. Since the electrical resistance did not change, there was also not a drastic change in the electrical conductivity of their supernatant when compared with the original plasma solutions, and as such formed a weaker "hard" corona, thereby not being able to entrap the counterions well in the corona shell.

We further attempted to analyze these corona complexes obtained by using physiochemical characterization techniques that have been utilized to characterize the corona complexes in the past such as dynamic light scattering, zeta potential, excitation–emission profiles, 1D SDS-PAGE, which corroborate with our integrated microfluidic/resistance setup. We attempted to study the composition of the corona complexes and how the "synthetic identity" plays a role in the formation of the corona, by carrying out LC-MS experiments and further classified the proteins according to their function in blood namely complement activation, immune response, coagulation, acute phase, lipoproteins, and tissue leakage.

In future, the proposed integrated microfluidic-based characterization technique has potential to be utilized to investigate protein corona complex formation for more extensively studied NP platforms such as gold NPs, silica NPs, iron oxide NPs, etc. [68–72] and monitor "soft" or "hard" corona complexes getting formed, correlating with their "synthetic identity." This would eventually lead to the development of a comprehensive database consisting of multiple NPs classified as capable of forming thicker or weaker "hard" corona based on their measured resistance values in a similar time-resolved manner. Having such a database could be useful for developing a semiquantitative relationship that would potentially be able to predict these bio–nano interactions and their subsequent biological fates in vivo.

4. Experimental Section

Materials: Sucrose, PEG (Mw = 10 K), branched PEI (average Mw ≈25 000), were purchased from Sigma-Aldrich (MO, USA). Lecithin (Zw) was purchased from NOF Corporation and used without further purification. Plasma protein as referred throughout the work was lyophilized human plasma purchased from Sigma-Aldrich (P9523 SIGMA) and dissolved in 5 mL PBS 1× and stored in small batches (200 μL vials). Each vial was thawed at 4 °C before running each experiment. P9523 SIGMA was prepared from whole blood that was collected with anticoagulants (9:1) from centrifuged to remove cells and cellular debris. P9523 SIGMA was prepared from pooled human blood and contained 4% sodium citrate as an anticoagulant. It was tested for clotting, which implied that the clotting factors were active.

Synthesis of Carbon Nanoparticles and Purification: Pristine CNPs were prepared by dissolving 200 mg of sucrose in 2 mL of nanopure water (0.2 × 10^{-6} M, 18 MΩ cm). Following this the aqueous solution was heated on a hot plate at 270 °C for ≈30 min and resuspended in 4 mL nanopure water, followed by 20 min of probe sonication (Q700 TM, Qsonica Sonicators, CT, USA) (Amp:1, on: 2, off: 1s). The solution was passed through a syringe filter with 0.22 μm pore size (Millex R, Merck Millipore Ltd., Ireland). The particles were then subjected to purification

by exhaustive dialysis against nanopure water (0.2 μm) using cellulose membrane (10 kDa MW CO).

For preparation of CNPs by prepassivation route (CNP–PEG, CNP–Zw), a mixture of sucrose and passivating polymer/lipid was taken in an empty 20 mL glass vial, to which 2 mL of nanopure water was added, and mixed well to form a homogeneous mixture. The concentration ratio of sucrose to passivating agent was maintained at 1:1 (w/w). For the nucleation process, the mixture was maintained at 270 °C, and the glass vial was kept uncapped to allow the slow evaporation of water. The temperature was maintained for 30 min, which generated brownish mass (color varied with the passivating agent). The mass was broken down with spatula and resuspended in 4 mL nanopure water, followed by 20 min of probe sonication (Q700 TM, Qsonica Sonicators, CT, USA) (Amp:1, on: 2, off: 1s). The sonicated suspension was centrifuged at 12 000 × g for 20 min, followed by collection of supernatants after filtration through a 0.22 μm syringe filter. The particles were then subjected to purification by exhaustive dialysis against nanopure water (0.2 μm) using cellulose membrane (10 kDa MW CO). Since PEG passivate onto CNPs by conjugating with free COOH groups present on the latter's surface, so to roughly estimate the functionalization percentage of PEG, the percentage of free COOH groups before and after passivation was calculated. By deconvolving the C1s spectra via XPS for CNP and CNP–PEG after which the percentage of COOH present in both was calculated which showed ≈44% surface coverage (Table S5, Supporting Information).

For preparation of CNPs by postpassivation route (CNP–PEI), a stock solution of branched PEI stock solution (1 mg 10 μL^{-1}) was made. Following this, 10 μL of this stock was added to 1 mg of CNP to make CNP–PEI). The solution was vortex vigorously for 5 min, and incubated at room temperature for 30 min, followed by centrifugation for 30 min at 75 000 rpm at 4C (Optima MAX-XP Ultracentrifuge, Beckman-Coulter, CA, USA) to remove the suspension. The collected pellet was then redispersed in nanopure water and probe-sonicated for 2 min (Amp: 1, on: 2s, off: 1s). All prepared CNPs were freeze dried and made at the same concentration of 1 mg mL^{-1}.

Nanoparticle Tracking Analysis: Nanoparticle hydrodynamic size, size distribution, and concentration were determined by NTA using a Malvern Technologies NanoSight NS300 system configured with a 488 nm laser and a high sensitivity scientific CMOS camera. Samples (5 μL of CNPs in 995 μL of phosphate buffered saline) were diluted according to manufacturer's recommendations for these measurements. For each measurement, five 1 min videos were recorded under the following conditions: temperature: 25 °C; flow rate = 100. Autofocus was adjusted to avoid indistinct particles. After recording, the captured videos were analyzed using in-built NanoSight Software with a detection threshold of 5.

Dynamic Light Scattering: Hydrodynamic size distributions of the nanoparticles were determined through dynamic light scattering measurements on a Malvern Zetasizer ZS90 instrument (Malvern Instruments Ltd., United Kingdom) at a fixed angle of 90°. 10 mL of the particle suspension was mixed with 990 mL of phosphate buffered saline (pH 7.4) before running the samples in the DLS machine. A photomultiplier aperture of 400 nm was used, and the incident laser power was adjusted to obtain a photon counting rate between 200 and 300 kcps. Measurements for which the measured and calculated baselines of the intensity autocorrelation function were within 0.1% range were used for calculating the diameter. All measurements were performed in triplicates of 13 consecutive measurements.

Transmission Electron Microscopy: TEM grids were prepared by drop casting 2.5 μL of the undiluted liquid CNP solution on carbon-coated copper grids (Ted Pella Inc.), and excess moisture was wicked away after 2 min. An acceleration voltage of 20 keV was used. Nanoparticle size analysis was conducted in ImageJ. Images were smoothed, and contrast was adjusted as necessary for separation of nanoparticles from the background. The hydrodynamic diameters of CNPs passivated with PEG was found to be different than the other CNPs, which can be attributed to the larger bushy chains, which were extended once these particles were suspended in aqueous media. On the other hand, a more tightly

**ADVANCED
SCIENCE NEWS**

www.advancedsciencenews.com

**small
methods**

www.small-methods.com

wrapped thin layer of the polymer was envisioned for CNP–PEI. The anhydrous diameter from TEM studies revealed that the anhydrous diameter for bare CNP to be 3 nm, whereas for CNP–PEG to be 6 nm (at least 20 CNPs per image). However, their hydrodynamic diameter was found to be ≈10 and 12 nm, respectively, for CNP–PEG and CNP–PEI samples. As evident from earlier studies, TEM measurements of CNPs are challenging due to their lack of inherent contrast. Discrepancies between aqueous hydrodynamic sizes and anhydrous TEM diameter are also common as evident from similarly published works.[39,41,72–77] A plausible reason for such a difference between the hydrodynamic and anhydrous diameters could be due to formation of a layer of hydration in the hydrated state which gets removed when the samples are drop casting for measuring the anhydrous diameter via TEM.

Zeta Potential: Zeta potential (ζ) values were determined using Malvern Zetasizer instrument (Malvern Instruments, UK) of the Nano series. The experiments were performed in phosphate buffered saline (pH 7.4) at 25 °C using the light scattering mode of the phase analysis light scattering (PALS) system following solution equilibration. The Smoluchowski equation was used to calculate ζ from the electrophoretic mobility (μ) of the measured nanoparticles as follows: $\mu = \varepsilon\zeta/\eta$, where ε and η are the dielectric constant and the absolute viscosity of the medium, respectively.

Excitation–Emission Profiles: The emission spectra for fluorescence measurements were recorded using the NanoDrop 3300 Fluorospectrometer (Thermo Scientific, MA, USA). The excitation wavelength was set to 365 nm and the wavelength covered an emission range of 400–750 nm.

Fabrication of a Microfluidic Device with Integrated Micro-Au Electrodes: This work utilized three steps process to fabricate a microfluidic device: 1) Developing of microchannel template on Si wafer using a soft photolithography procedure. 2) Evaporating of micro-Au electrodes on indium tin oxide (ITO) coated glass. 3) Transferring microfluidic pattern to polydimethylsiloxane (PDMS) layer and bonding with ITO glass. Briefly, the process started with spinning SU-8 photoresist onto bare preheated Si wafer at 150 rpm for 45 s and 450 rpm for 120 s. After spinning, prebaking was done at 95 °C for 20 min followed 2 min at RT. Soft photolithography was employed with prepattern mask for 3 min at RT. Postbaking procedure was then demonstrated at 110 °C for 15 min followed by 3 min at RT. Finally, the Si wafer with coated microfluidic template was dipped in SU-8 developer for 20 min until the pattern was clearly visible. An optical microscope was used to analyze each step. Constant stirring was provided during developing step. Finally, the sample was dried using nitrogen spray gun for 5 min. The developed microfluidic pattern was then transferred to PDMS layer. A 10:1 (w/w) mixture of Sylgard 184 PDMS elastomer base and curing agent (Dow Corning Corporation, Midland, MI, USA) was poured on preformed microchannel pattern on Si wafer and degassed in a dissector under vacuum for 1 h a RT. This process ensured removing of any bubble created during a mixing procedure. The Si device with cured PDMS was finally heated at 100°C for 1 h. PDMS with transferred pattern was peeled off carefully and stored until further use. ITO coated glass was purchased from Sigma-Aldrich and cleaned with standard Radio Corporation of America (RCA) procedure. Electron beam evaporator was employed using a prepattern shadow mask to evaporate micro-Au electrodes with dimension (thickness of 30 nm, width of 30 nm and interspacing between two electrodes of 50 nm). Finally, plasma activation was used for 15 min to bond the ITO glass with micro-Au electrodes with PDMS. Using plasma treatment, reactive species such as ions and radicals were generated which attacked the siloxane backbone of PDMS to form oxygen rich SiO_x silica like layer and Si–OH surface structures, making it hydrophilic instead of hydrophobic and minimizing the nonspecific protein interactions with PDMS.[78]

Microfluidic Setup, Particle Incubation, and Real-Time Monitoring: Three microfluidic devices connected in series tubing (Cole Parmer Instrument Company, Vernon Hills, Illinois, USA) were interfaced with a mechanical pump Chemyx, Inc. Fusion 200 (Chemyx Inc., Stafford, TX, USA) to setup a variable controlled flow rate for pristine CNP, CNP–Zw, CNP—PEI, and CNP–PEG before (5 µL min⁻¹) and after (10 µL min⁻¹) interaction with plasma proteins. Evaporated Au electrodes pads were

connected to impedance analyzer to record the base impedance and the change in impedance of CNP, CNP–Zw, CNP–PEI, and CNP–PEG before and after interaction with plasma proteins at different time intervals. Samples were collected from each microfluidic device at dedicated outlets (Figure S10, Supporting Information) and were further characterized utilizing standard techniques to analyze the protein corona formation at different stages.

Scanning Electron Microscopy: SEM was used to analyze the morphology and surface topography of the engraved channels. Prior to imaging, engraved PDMS microfluidic chips were washed and sonicated with acetone, isopropanol (IPA), and deionized (DI) water for 2 min each, to eliminate any polymer or dust particle residues. The chips were further dried with clean Nitrogen (N_2) gas and stored under vacuum. Clean microfluidic devices were mounted on a SEM sample holder using a piece of carbon tape and gold-coated via sputtering for 60 s at 20 mA. The images were obtained using a Hitachi (Schaumburg, Illinois) S-4800 SEM with Oxford Instruments (Abingdon, Oxfordshire). Imaging was performed in a long working distance mode, with an accelerating voltage of 10 kV, extracting current of 10 µA, and working distance of 25 mm for scanning.

Separation of Protein in the Corona by 1D SDS-PAGE: Proteins surrounding the NPs were dissolved in Laemmle buffer and heated for 10 min at 90 °C before being loaded and resolved onto 12% Mini-PROTEAN TGX precast gels (Bio-Rad Laboratories, Hercules, CA, USA) for 1.5 h at 130 V. Proteins were stained with Coomassie Brilliant Blue (Fisher Scientific, Fair Lawn, NJ, USA) overnight followed by extensive washing. For a particular CNP/protein complex at a particular time-point, experiments were performed in triplicates.

Protein Digest Preparation and LC-MS Analysis of Tryptic Digests: Coomassie stain was removed from the gel pieces with successive washes of acetonitrile (ACN), 50×10^{-3} M ammonium bicarbonate, and 50% ACN in 50×10^{-3} M ammonium bicarbonate. After destaining, the gel pieces were dried in a vacuum centrifuge. Next, 10×10^{-3} M tris(2-carboxyethyl) phosphine hydrochloride (TCEP) was added for incubation at 25 °C for 30 min; this was followed by a 30 min incubation with 40×10^{-3} M chloroacetamide (CAA) to alkylate the disulfide bonds reduced by TCEP. The gel pieces were then dehydrated with ACN, dried briefly, and reswelled in buffer containing 1.5 µg of proteomics-grade trypsin. Proteins were digested overnight at 37 °C, and on the next day, peptides were extracted with several aliquots of 5% formic acid (FA) in 50% ACN. The peptide samples were finally desalted using StageTips[1] and dried to completion.

Dried peptide samples were suspended in 0.1% FA in 5% ACN and injected into an UltiMate 3000 UHPLC system. Reversed phase separation of sample peptides was accomplished using a 15 cm Acclaim PepMap 100 C18 column with mobile phases of 0.1% FA in ultrapure water (A) and 0.1% FA in ACN (B). Peptides were eluted using a gradient of 5% B to 60% B over 60 min. The UHPLC system was coupled online to a high resolution Thermo Orbitrap Fusion Tribrid mass spectrometer operated in the data dependent mode. Precursor scans from 300 to 1500 m/z (120 000 resolution, 2e5 AGC) were followed by collision induced dissociation (CID) of the most abundant precursors over a maximum cycle time of 3 s with a normalized collision energy of 35% (1e4 AGC). The isolation window was set to 1.6 m/z, while the dynamic exclusion window was fixed at 60 s.

The raw data was analyzed using Mascot 2.5.1 against the SwissProt *Homo sapiens* protein database (20245 nonredundant sequences). Full tryptic digestion was specified with a maximum of three missed cleavages. Peptide mass tolerance and fragment mass tolerance were set to 10 ppm and 0.3 Da, respectively. Variable modifications included oxidation of methionine residues, carbamidomethylation of cysteine residues, and acetylation of protein N-termini.

Protein Digest Preparation and LC-MS Analysis of Tryptic Digests: For each protein, exponentially modified protein abundance indices (emPAI) were determined by Mascot as emPAI = $10N_{obsd}/N_{obsl} - 1$; where N_{obsd} is the number of observed unique peptides, and N_{obsl} is the number of all possible unique peptides calculated from each protein. Protein contents in molar fraction percentages (mol%) were computed from emPAI as

$mol\% = 100$ emPAI$_i$/Σ_i emPAI, where emPAI$_i$ is the emPAI value for a given protein (i) in a protein list (any above score greater than or equal to 50) for a particular CNP–protein corona complex and Σ_i emPAI is the sum of all emPAI values pertaining to that particular CNP–plasma protein complex.

Statistical Analysis: Statistics were computed with GraphPad Prism 7. Statistical significance was determined as appropriate by Mann–Whitney test or one-way or two-way ANOVA with Bonferroni post-test for single or multiple comparisons. A value of $p < 0.05$ was considered as statistically significant.

Supporting Information

Supporting Information is available from the Wiley Online Library or from the author.

Conflict of Interest

Prof Pan is the founder/co-founder of three university based start-ups. None of these entities, however, supported this work.

[1] P. Turbill, T. Beugeling, A. A. Poot, *Biomaterials* **1996**, *17*, 1279.
[2] E. Casals, T. Pfaller, A. Duschl, G. J. Oostingh, V. Puntes, *ACS Nano* **2010**, *4*, 3623.
[3] D. Docter, D. Westmeier, M. Markiewicz, S. Stolte, S. K. Knauer, R. H. Stauber, *Chem. Soc. Rev.* **2015**, *44*, 6094.
[4] S. Tenzer, D. Doctor, J. Kuharev. A. Musyanovych, V. Fetz, R. Hecht, F. Schlenk, D. Fischer, K. Kiouptsi, C. Reinhardt, K. Landfester, H. Schild, M. Maskos, S. K. Knauer, R. H. Stauber, *Nat. Nanotechnol.* **2013**, *8*, 772.
[5] F. Chen, G. Wang, J. I. Griffin, B. Brenneman, N. K. Banda, V. M. Holers, D. S. Backos, L. P. Wu, S. M. Moghimi, D. Simberg, *Nat. Nanotechnol.* **2017**, *12*, 387.
[6] R. C. Murdock, L. Braydich-Stolle, A. M. Schrand, J. J. Schlager, S. M. Hussain, *Toxicol. Sci.* **2008**, *101*, 239.
[7] T. L. Moore, L. Rodriguez-Lorenzo, V. Hirsch, S. Balog, D. Urban, C. Jud, B. Rothen-Rutishauser, M. Lattuada, A. Petri-Fink, *Chem. Soc. Rev.* **2015**, *44*, 6287.
[8] M. Falahati, F. Attar, M. Sharifi, T. Haertlé, J.-F. Berret, R. H. Khan, A. A. Saboury, *Biochim. Biophys. Acta, Gen. Subj.* **2019**, *1863*, 971.
[9] K. L. Aillon, Y. M. Xie, N. El-Gendy, C. J. Berkland, M. L. Forrest, *Adv. Drug Delivery Rev.* **2009**, *61*, 457.
[10] P. P. Adiseshaiah, J. B. Hall, S. E. McNeil, *Wiley Interdiscip. Rev.: Nanomed. Nanobiotechnol.* **2010**, *2*, 99.
[11] J. Leszczynski, *Nat. Nanotechnol.* **2010**, *5*, 633.
[12] S. Tenzer, D. Docter, S. Rosfa, A. Wlodarski, J. Kuharev, A. Rekik, S. K. Knauer, C. Bantz, T. Nawroth, C. Bier, J. Sirirattanapan, W. Mann, L. Treuel, R. Zellner, M. Maskos, H. Schild, R. H. Stauber, *ACS Nano* **2011**, *5*, 7155.
[13] M. Neagu, Z. Piperigkou, K. Karamanou, A. B. Engin, A. O. Docea, C. Constantin, C. Negrei, D. Nikitovic, A. Tsatsakis, *Arch. Toxicol.* **2017**, *91*, 1031.
[14] T. Cedervall, I. Lynch, S. Lindman, T. Berggard, E. Thulin, H. Nilsson, K. A. Dawson, S. Linse, *Proc. Natl. Acad. Sci. USA* **2007**, *104*, 2050.
[15] M. Lundqvist, J. Stigler, G. Elia, I. Lynch, T. Cedervall, K. A. Dawson, *Proc. Natl. Acad. Sci. USA* **2008**, *105*, 14265.
[16] L. Treuel, S. Brandholt, P. Maffre, S. Wiegele, L. Shang, G. U. Nienhaus, *ACS Nano* **2014**, *8*, 503.
[17] P. C. Ke, S. Lin, W. J. Parak, T. P. Davis, F. Caruso, *ACS Nano* **2017**, *11*, 11773.
[18] O. Vilanova, J. J. Mittag, P. M. Kelly, S. Milani, K. A. Dawson, G. Franzese, *ACS Nano* **2016**, *10*, 10842.
[19] N. Bertrand, P. Grenier, M. Mahmoudi, E. M. Lima, E. A. Appel, F. Dormont, J. M. Lim, R. Karnik, R. Langer, O. C. Farokhzad, *Nat. Commun.* **2017**, *8*, 777.
[20] S. Li, Z. Peng, R. M. Leblanc, *Anal. Chem.* **2015**, *87*, 6455.
[21] M. Wang, C. Fu, Z. Liu, N. Yang, S. Yu, *Nanoscale* **2015**, *7*, 15191.
[22] M. Assfalg, L. Ragona, K. Pagano, M. D'Onofrio, S. Zanzoni, S. Tomaselli, H. Molinari, *Biochim. Biophys. Acta, Proteins Proteomics* **2016**, *1864*, 102.
[23] M. Carril, D. Padro, P. del Pino, C. Carrillo-Carrion, M. Gallego, W. J. Parak, *Nat. Commun.* **2017**, *8*, 1542.
[24] D. J. O'Connell, F. B. Bombelli, A. S. Pitek, M. P. Monopoli, D. J. Cahill, K. A. Dawson, *Nanoscale* **2015**, *7*, 15268.
[25] N. Fernández-Iglesias, J. Bettmer, *Nanoscale* **2015**, *7*, 14324.
[26] R. Capomaccio, I. Ojea-Jimenez, P. Colpo, D. Gilliland, G. Ceccone, F. Rossi, L. Calzolai, *Nanoscale* **2015**, *7*, 17653.
[27] S. Milani, F. B. Bombelli, A. S. Pitek, K. A. Dawson, J. Rädler, *ACS Nano* **2012**, *6*, 2532.
[28] D. Walczyk, F. B. Bombelli, M. P. Monopoli, I. Lynch, K. A. Dawson, *J. Am. Chem. Soc.* **2010**, *132*, 5761.
[29] M. Mahmoudi, S. E. Lohse, C. J. Murphy, A. Fathizadeh, A. Montazeri, K. S. Suslick, *Nano Lett.* **2014**, *14*, 6.
[30] S. Ritz, S. Schöttler, N. Kotman, G. Baier, A. Musyanovych, J. Kuharev, K. Landfester, H. Schild, O. Jahn, S. Tenzer, V. Mailander, *Biomacromolecules* **2015**, *16*, 1311.
[31] S. Galmarini, U. Hanusch, M. Giraud, N. Cayla, D. Chiappe, N. von Moos, H. Hofmann, L. Maurizi, *Bioconjugate Chem.* **2018**, *29*, 3385.
[32] S. Palchetti, V. Colapicchioni, L. Digiacomo, G. Caracciolo, D. Pozzi, A. L. Capriotti, G. L. Barbera, A. Lagana, *Biochim. Biophys. Acta, Biomembr.* **2016**, *1858*, 189.
[33] K. Yu, P. Andruschak, H. H. Yeh, D. Grecov, J. N. Kizhakkedathu, *Biomaterials* **2018**, *166*, 79.
[34] L. Digiacomo, S. Palchetti, F. Giulimondi, D. Pozzi, R. Z. Chiozzi, A. L. Capriotti, A. Lagana, G. Caracciolo, *Lab Chip* **2019**, *19*, 2557.
[35] A. C. G. Weiss, K. Kruger, Q. A. Besford, M. Schlenk, K. Kempe, S. Forster, F. Caruso, *ACS Appl. Mater. Interfaces* **2019**, *11*, 2459.
[36] W. J. Polacheck, R. Li, S. G. M. Uzel, R. D. Kamm, *Lab Chip* **2013**, *13*, 2252.

**ADVANCED
SCIENCE NEWS**

www.advancedsciencenews.com

**small
methods**

www.small-methods.com

[37] K. Namdee, A. J. Thompson, P. Charoenphol, O. Eniola-Adefeso, *Langmuir* **2013**, *29*, 2530.

[38] A. C. G. Weiss, K. Kempe, S. Föster, F. Caruso, *Biomacromolecules* **2018**, *19*, 2580.

[39] I. Srivastava, S. K. Misra, F. Ostadhossein, E. Daza, J. Singh, D. Pan, *Nano Res.* **2017**, *10*, 3269.

[40] S. K. Misra, I. Srivastava, I. Tripathi, E. A. Daza, F. Ostadhossein, D. Pan, *J. Am. Chem. Soc.* **2017**, *139*, 1746.

[41] S. K. Misra, I. Srivastava, J. S. Khamo, V. V. Krishnamurthy, D. Sar, A. S. Schwartz-Duval, J. Soares, K. Zhang, D. Pan, *Nanoscale* **2018**, *10*, 18510.

[42] U. Hassan, T. Ghonge, B. Reddy Jr., M. Patel, M. Rappleye, I. Taneja, A. Tanna, R. Healey, N. Manusry, Z. Price, T. Jensen, J. Berger, A. Hasnain, E. Flaugher, S. Liu, B. Davis, J. Kumar, K. White, R. Bashir, *Nat. Commun.* **2017**, *8*, 15949.

[43] T. Ghonge, A. Ganguli, E. Valera, M. Saadah, G. L. Damhorst, J. Berger, G. P. Diaz, U. Hassan, M. Chheda, Z. Haidry, S. Liu, C. Hwu, R. Bashir, *APL Bioeng.* **2017**, *1*, 016103.

[44] E. Valera, J. Berger, U. Hassan, T. Ghonge, J. Liu, M. Rappleye, J. Winter, D. Abboud, Z. Haidry, R. Healey, N. T. Hung, N. Leung, N. Mansury, A. Hasnain, C. Lannon, Z. Price, K. White, R. Bashir, *Lab Chip* **2018**, *18*, 1461.

[45] B. O'Shaughnessy, Q. Yang, *Phys. Rev. Lett.* **2005**, *94*, 048302.

[46] L. Digiacomo, F. Cardarelli, D. Pozzi, S. Palchetti, M. A. Digman, E. Gratton, A. L. Capriotti, M. Mahmoudi, G. Caracciolo, *Nanoscale* **2017**, *9*, 17254.

[47] D. F. Moyano, K. Saha, G. Prakash, B. Yan, H. Kong, M. Yazdani, V. M. Rotello, *ACS Nano* **2014**, *8*, 6748.

[48] J. F. Affonso de Oliveira, F. R. Scheffer, R. F. Landis, E. T. Neto, V. M. Rotello, M. B. Cardoso, *ACS Appl. Mater. Interfaces* **2018**, *10*, 41917.

[49] Q. Dai, C. Walkey, W. C. W. Chan, *Angew. Chem., Int. Ed.* **2014**, *53*, 13493.

[50] C de Boor, *Applied Mathematical Sciences*, Vol. *27*, Springer-Verlag, New York **1978**.

[51] *Mathematica, Version 11.3*, Wolfram Research, Inc., Champaign, IL **2018**.

[52] W. Qiao, H. H. Sun, W. Y. Chey, K. Y. Lee, *Ann. Biomed. Eng.* **1998**, *26*, 1072.

[53] L. F. Chalak, F. Tian, B. Adams-Huet, D. Vasil, A. Laptook, T. Tarumi, R. Zhang, *Sci. Rep.* **2017**, *7*, 45958.

[54] E. L. Blundell, M. J. Healey, E. Holton, M. Sivakumaran, S. Manstana, M. Platt, *Anal. Bioanal. Chem.* **2016**, *408*, 5757.

[55] S. Milani, F. Baldelli Bombelli, A. S. Pitek, K. A. Dawson, J. Rädler, *ACS Nano* **2012**, *6*, 2532.

[56] L. Shang, G. U. Nienhaus, *Acc. Chem. Res.* **2017**, *50*, 387.

[57] Y. Jeong, J. Lee, J. Moon, J. H. Shin, W. D. Lu, *Nano Lett.* **2018**, *18*, 4447.

[58] F. Daeyaert, F. Ye, M. W. Deem, *Proc. Natl. Acad. Sci. USA* **2019**, *116*, 3413.

[59] C. C. Fleischer, C. K. Payne, *J. Phys. Chem. B* **2012**, *116*, 8901.

[60] C. C. Fleischer, C. K. Payne, *Acc. Chem. Res.* **2014**, *47*, 2651.

[61] M. Lundqvist, J Stigler, T. Cedervall, T. Berggråd, M. B. Flanagan, I. Lynch, G. Elia, K. Dawson, *ACS Nano* **2011**, *5*, 7503.

[62] T. Cedervall, I. Lynch, M. Foy, T. Berggård, S. C. Donnelly, G. Cagney, S. Linse, K. A. Dawson, *Angew. Chem., Int. Ed.* **2007**, *46*, 5754.

[63] B. D. Johnston, W. G. Kreyling, C. Pfeiffer, M. Schaffler, H. Sarioglu, S. Ristig, S. Hirn, N. Haberl, S. Thalhammer, S. M. Hauck, M. Semmler-Behnke, M. Epple, J. Hühn, P. d. Pino, W. J. Parak, *Adv. Funct. Mater.* **2017**, *27*, 1701956.

[64] E. Mahon, A. Salvati, F. Baldelli Bombelli, I. Lynch, K. A. Dawson, *J. Controlled Release* **2012**, *161*, 164.

[65] S. Schöttler, G. Becker, S. Winzen, T. Steinbach, K. Mohr, K. Landfester, V. Mailander, F. R. Wurm, *Nat. Nanotechnol.* **2016**, *11*, 372.

[66] Y. Ishihama, Y. Oda, T. Tabata, T. Sato, T. Nagasu, J. Rappsilber, M. Mann, *Mol. Cell. Proteomics* **2005**, *4*, 1265.

[67] Y. Yan, K. T. Gause, M. M. J. Kamphuis, C.-S. Ang, N. M. O'Brien-Simpson, J. C. Lenzo, E. C. Reynolds, E. C. Nice, F. Caruso, *ACS Nano* **2013**, *7*, 10960.

[68] A. A. Saei, M. Yazdani, S. E. Lohse, Z. Bakhtiary, V. Serpooshan, M. Ghavami, M. Asadian, S. Mashaghi, E. C. Dreaden, A. Mashaghi, M. Morteza, *Chem. Mater.* **2017**, *29*, 6578.

[69] J. W. Park, J. S. Shumaker-Parry, *J. Am. Chem. Soc.* **2014**, *136*, 1907.

[70] T. H. Chung, S. H. Wu, M. Yao, C. W. Lu, Y. S. Lin, Y. Hung, C. Y. Mou, Y. C. Chen, D. M. Huang, *Biomaterials* **2007**, *28*, 2959.

[71] M. Mahmoudi, S. Laurent, M. A. Shokrgozar, M. Hosseinkhani, *ACS Nano* **2011**, *5*, 7263.

[72] S. K. Misra, H. H. Chang, P. Mukherjee, S. Tiwari, A. Ohoka, D. Pan, *Sci. Rep.* **2015**, *5*, 14986.

[73] I. Srivastava, D. Sar, P. Mukherjee, A. S. Schwartz-Duval, Z. Huang, C. Jaramillo, A. Civantos, I. Tripathi, J. P. Allain, R. Bhargava, D. Pan, *Nanoscale* **2019**, *11*, 8226.

[74] I. Srivastava, J. S. Khamo, S. Pandit, P. Fathi, X. Huang, A. Cao, R. T. Haasch, S. Nie, K. Zhang, D. Pan, *Adv. Funct. Mater.* **2019**, *29*, 1902466.

[75] S. Pandit, T. Banerjee, I. Srivastava, S. Nie, D. Pan, *ACS Sens.* **2019**, *4*, 2730.

[76] H. Liu, Z. Li, Y. Sun, X. Geng, Y. Hu, H. Meng, J. Ge, L. Qu, *Sci. Rep.* **2018**, *8*, 1086.

[77] N. Papaioannou, A. Marinovic, N. Yoshizawa, A. E. Goode, M. Fay, A. Khlobystov, M.-M. Titirici, A. Sapelkin, *Sci. Rep.* **2018**, *8*, 6559.

[78] D. C. Duffy, J. Cooper McDonald, O. J. A. Schueller, G. M. Whitesides, *Anal. Chem.* **1998**, *70*, 4974.